(2)

TECHNICAL REPORT BRL-TR-3392

BRL

MATERIAL MODELING FOR TERMINAL BALLISTIC SIMULATION

G. HAUVER
N. HUFFINGTON
K. KIMSEY
L. MAGNESS
M. RAFTENBERG
G. RANDERS-PEHRSON
M. SCHEIDLER
S. SEGLETES
J. WALTER
T. WRIGHT

EDITED BY J. WALTER

SEPTEMBER 1992

U.S. ARMY LABORATORY COMMAND

BALLISTIC RESEARCH LABORATORY
ABERDEEN PROVING GROUND, MARYLAND

DISCLAIMER NOTICE

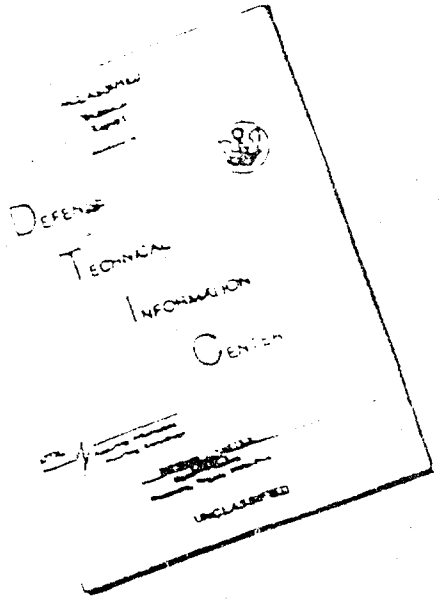

THIS DOCUMENT IS BEST QUALITY AVAILABLE. THE COPY FURNISHED TO DTIC CONTAINED A SIGNIFICANT NUMBER OF PAGES WHICH DO NOT REPRODUCE LEGIBLY.

REPORT DOCUMENTATION PAGE

Form Approved
OMB No 0704-0188

1. AGENCY USE ONLY (Leave blank)	2. REPORT DATE	3. REPORT TYPE AND DATES COVERED
	September 1992	Final, Sep 91–June 92

4. TITLE AND SUBTITLE
Material Modeling for Terminal Ballistic Simulation

5. FUNDING NUMBERS
PR: 1L161102AH43

6. AUTHOR(S)
G. Hauver, N. Huffington, K. Kimsey, L. Magness, M. Raftenberg, G. Randers-Pehrson, M. Scheidler, S. Segletes, J. Walter, T. Wright

7. PERFORMING ORGANIZATION NAME(S) AND ADDRESS(ES)

8. PERFORMING ORGANIZATION REPORT NUMBER

9. SPONSORING/MONITORING AGENCY NAME(S) AND ADDRESS(ES)
U.S. Army Ballistic Research Laboratory
ATTN: SLCBR-DD-T
Aberdeen Proving Ground, MD 21005-5066

10. SPONSORING/MONITORING AGENCY REPORT NUMBER
BRL-TR-3392

11. SUPPLEMENTARY NOTES
Edited by J. Walter

12a. DISTRIBUTION/AVAILABILITY STATEMENT
Approved for public release; distribution is unlimited.

12b. DISTRIBUTION CODE

13. ABSTRACT (Maximum 200 words)

Numerical simulation of terminal ballistic events requires quantitative modeling of the complex material responses which are observed to occur experimentally. This report discusses current deficiencies and future needs for material modeling in this context and suggests some specific efforts which, in the opinion of the authors, could substantially improve the utility of simulation as a design and analysis tool for armor/anti-armor systems.

14. SUBJECT TERMS
terminal ballistics, armor, anti-armor ammunition, numerical methods, material modeling

15. NUMBER OF PAGES
98

16. PRICE CODE

17. SECURITY CLASSIFICATION OF REPORT	18. SECURITY CLASSIFICATION OF THIS PAGE	19. SECURITY CLASSIFICATION OF ABSTRACT	20. LIMITATION OF ABSTRACT
UNCLASSIFIED	UNCLASSIFIED	UNCLASSIFIED	SAR

Contents

List of Figures

Director's Foreward

Several months ago I asked a group of BRL scientists and engineers to put together a "White Paper" on the knowledge gaps that most seriously deter our ability for analytical and computational prediction of phenomena in armor, penetration, and warhead mechanics. My purpose was to gain focus for our internal efforts and to express our needs to others who might join our quest. I am optimistic that others will do so since our needs are not unique. I am sure that many will recognize that we will accomplish more by cooperative, focused effort then we could do separately.

This document is the result of my request. It overwhelmingly exceeds my expectations which were for a summary list with a brief rationalization for each. It provides focus for specific, priority work and also gives a broad perspective as context for these needs.

My hope is that this will be a living document that is nurtured by the BRL and by the community at large confronted with problems involving material response at extremes of load and deformation and their rates. I am certain it will prove invaluable if it helps to maintain an evolving focus on our collective needs. I invite everyone involved in the challenging problems represented here to join with us in defining and maintaining this focus.

INTENTIONALLY LEFT BLANK.

Preface (T. Wright)

Historical Remarks Just over a decade ago the National Materials Advisory Board (NMAB) published a report entitled "Materials Response to Ultra-High Loading Rates" [1]. This report surveyed the state of material modeling then in existence, as appropriate for analysis and design of conventional ordnance devices. By way of background, NMAB-356 came into existence because it was widely recognized by the mid 1970's that inadequate description of severe deformation and failure in solids constituted a major limitation on the effectiveness of large scale computations in ordnance applications. Three years prior to publication of the report, at the urging of the Ballistic Research Laboratory (BRL) and the Army Research Office (ARO), the office of the Director of Defense Research and Engineering (DDR&E, DOD) had requested NMAB to assess the state of the art as it existed at that time, and to recommend future directions for research and development. Consequently an expert committee, drawn from academia and from both private and government research laboratories, was formed, and after a series of meetings, NMAB-356 was born.

For various reasons the committee confined itself to a discussion of metals only. At the risk of gross oversimplification, some of the major points that emerged may be summarized as follows. In decreasing order of importance, limitations in the state of material modeling were found to be:

1. severe in dynamic material failure;
2. moderate in plastic deformation;
3. trivial for most purposes in equations of state.

Recommended research emphasized: nucleation, growth, and coalescence of voids in ductile materials and of cracks in brittle materials; all aspects of the formation and propagation of adiabatic shear bands; and development of the underlying micromechanics, thermodynamics, and kinematics of plastic deformation within the context of a consistent, finite deformation theory. The report also suggested the development of new test methods for high rate deformation and failure. The interested reader is referred to the original report for many fascinating details and partial analyses, which in toto give a vivid snapshot of the state of the art in dynamic material modeling circa 1980. NMAB-356 served as a catalyst and rationale for much new work that was initiated in the early years of the decade following its publication, particularly in the area of adiabatic shear bands. Predictably, research in the academic and defense communities did not develop precisely along the lines called for, but on the whole NMAB-356 was a remarkably prescient document.

Purpose Today, twelve years later, as the tremendous advances in computing power made during the 1980's continue to accelerate, it is feasible to devote

an increasing fraction of the computing cycle to the evaluation of more sophisticated constitutive laws. Therefore, it seems appropriate to reassess our needs in the area of material modeling for terminal ballistic computation and analysis. Toward this end, this report presents an overview of the current state of material modeling in terminal ballistics codes and, perhaps more importantly, describes those deficiencies in the state of material modeling which are perceived to impose the most severe limitations on the capability and reliability of terminal ballistic simulation. Conversely, this report is *not* intended to be a comprehensive treatise on either terminal ballistics or the dynamic response of solids in general. The point of view expressed is that of a collection of professionals within the Terminal Ballistics Division of the Ballistic Research Laboratory, and therefore is by no means comprehensive.

User's Guide The report opens with a discussion of certain aspects of ballistic penetration from a phenomenological point of view. Extensive ballistic testing has demonstrated that adiabatic shear banding is a major mechanism for erosion of metals, and that it can often compete with bulk plastic flow in moving material away from the path of penetration. Similarly testing has demonstrated that transient effects from wave propagation must always be considered in brittle materials such as ceramics and cermets. The next section describes some of the major codes, as well as the principal material models, that are in use today for simulation of terminal effects. The next four sections deal with specific research areas that seem to have particular relevance today. Section 3 covers in-house and related efforts in finite plasticity, section 4 describes recent results in modeling adiabatic shear bands, section 5 is concerned with brittle failure and granular flow, and section 6 points out some problems with equations of state as they are actually used in todays impact codes. The report closes with a summary of important points that have arisen in the body of the report and a statement of needs that address those same points.

Closure and Call for Comments Clearly the major concerns of NMAB-356 are still of interest today. Failure is still the least understood aspect of material response, and therefore is receiving the most attention. However, failure in metals is preceded by finite plastic deformation, which determines the history and sets the environment within which damage and failure evolve. Analogously, transient wave propagation creates damage in brittle materials which sets the environment from which subsequent comminution evolves. Increased use of ceramics has brought recognition that post failure response is also important, hence the interest in granular flows. Finally, it seems that even as mature a subject as modeling of equations of state requires some care and attention.

Interested readers are invited to communicate their views on any and all aspects of this report to:

Director
Ballistic Research Laboratory
Attn: SLCBR-D
Aberdeen Proving Ground, Maryland 21005-5066.

INTENTIONALLY LEFT BLANK.

1 Phenomenology of Ballistic Penetration

1.1 Fundamentals of the Penetration Process (L. Magness)

The penetration of typical, ductile, metallic armor by a high-velocity kinetic energy penetrator (a rod-like projectile) or by the still higher velocity jet of metal produced by a shaped charge warhead can, to the first order, be viewed as a hydrodynamic process[1], as depicted in Figure 1. After a transient phase upon initial impact, the penetrator-target interaction quickly settles down to a nearly steady process in which the head of the impacting projectile or jet is eroded away at the penetrator-target interface, while the interface moves forward displacing a cavity in the armor. The kinetic energy of the impacting projectile or jet is expended primarily as plastic work, performed in opening a cavity in the armor material and eroding and inverting the penetrator itself. Very large peak stresses and plastic strain rates occur during the initial impact phase, but these levels quickly diminish to lower values during the much longer steady phase of the penetration process [2]. However, due to the deceleration of the incoming penetrator material at the penetrator-target interface and to the corresponding acceleration of the target material out of the path of the moving interface, the inertial forces developed during the steady-state phase will still greatly exceed the yield strengths of both the target and penetrator materials.

First order analytical penetration models treat the entire penetration process as simply a fluid-on-fluid interaction, Birkhoff [3]. An expression for the final depth of penetration, P, derived from the Bernoulli equation, results:

$$P = \sqrt{\rho_p/\rho_t}\, L, \tag{1}$$

where ρ_p and ρ_t are the mass densities of the penetrator and target materials respectively, and L is the length of the penetrator. This often gives quite reasonable penetration estimates for the performance of shaped charge jets, when L is corrected for stretching of the jet. With the inertial forces generated by the high velocities of jets dominating the penetration process, the penetration of ductile metallic targets thus becomes largely a function of jet density and length alone. This simple expression explains the use of high-ductility copper in shaped charge liners, to obtain stretching jets of greater lengths, and the use of high-density materials such as uranium and tantalum for shaped charge liners, and of uranium or tungsten for long-rod penetrators.

The fluid dynamic model is less applicable for impacts at somewhat lower velocities, such as the ordnance velocities of modern fin-stabilized, long rod penetrator munitions, or when the mechanical responses of the penetrator or target during

[1] It should be emphasized that penetration into a ceramic target produces a *very* different response than that discussed here; see Section 1.2

the penetration process are other than ductile erosion and cavity expansion, respectively. Additional terms representing the yield strengths of the penetrator and target materials are often included in modified versions of the Bernoulli equation to improve the representation of penetration events by these analytical models. The eroding-rod models (e.g. Tate [4, 5], Alekseevski [6], Frank and Zook [7]) which include these strength terms reflect the experimentally observed, velocity-dependent penetration of long-rod projectiles (Figure 2) and, when properly calibrated, can give reasonably accurate predictions of their overall penetration performance.

In the case of brittle materials (ceramics), the assumptions of the steady-state, hydrodynamic model must be questioned not only from the viewpoint of time-dependent strength degradation but also because experiments indicate a major contribution from transient wave interaction effects. This point is considered in more detail in the next section.

In reality, neither the penetrator nor the target materials behave as fluids or modified fluids. To better understand the penetration process, finite element or finite difference numerical simulations are employed. Two- and three-dimensional hydrocodes, both Eulerian and Lagrangian, attempt to model the actual deformation, flow, and fracture behavior of both penetrator and target materials. Through constitutive equations for each material, their mechanical responses under the high stress and high strain rate loading conditions are calculated and followed through each time increment of the penetration process. The ability of the numerical models to simulate the penetration event thus depends on the accuracy and completeness of the materials models and on the computational algorithms employed in the hydrocode itself. In the next section, several examples of some of the complexities of penetrator-target interactions which have been observed experimentally are given. Aspects of the mechanical responses of penetrator and target materials that have been shown to be important to the understanding and prediction of ballistic test results are illustrated by two phenomenological examples: (1) the penetration of hard ceramics, and (2) penetrations involving ductile materials, both armor and different high-density penetrator materials. In the subsequent sections, the ability of the computational hydrocodes to model these and other aspects of the penetration process will be reviewed and critiqued.

1.2 Phenomenological Observations of Penetration Into Brittle Materials (G. Hauver)

Ceramics are commonly assumed to have an inherent resistance to penetration by a long-rod projectile. However, test results often provide evidence that the ballistic performance of a ceramic-laminate target varies with time during the course of penetration. For example, increasing the proportion of ceramic in a target commonly fails to produce a corresponding improvement in its resistance

to penetration. In recent studies at the Ballistic Research Laboratory (BRL), all available data from quarter-scale ballistic tests were analyzed with the aid of a penetration model [4, 5] using the target resistance term, R, as a measure of ceramic performance. Such steady-state models are not intended to describe penetration when the resistance term is time dependent. However, the steady-state condition was satisfied by using a point-by-point analysis and assuming an average value of resistance from the beginning of penetration to a specific penetration depth in the ceramic of each test. This approach greatly suppressed the actual change in resistance during penetration, but it preserved performance trends which could be related to sources of damage to the ceramic that cause its R to change. Supporting tests were then conducted to identify features of target design which influenced the damage.

The analysis of quarter-scale ballistic tests indicated similar behavior for different ceramics, and representative performance trends are shown in Figure 3. In this figure, average resistance to penetration, R, is plotted as a function of time, T. With no cover plate at the front of the ceramic, performance typically followed Curve A. The performance was initially low, but it increased with time, passed through a maximum, and decreased at later times when different sources of damage became dominant. However, the decrease in performance at late times did not always occur. In one case [8] the performance continued to increase along Curve AA. This trend occurred when the ceramic, without a cover plate, was heavily confined at the back and side. With a steel cover plate, performance typically followed Curve B. The presence of a cover plate suppressed early damage, but the curve plunged rapidly as other damage sources influenced the performance. However, with efforts to suppress damage in tests at the BRL, performance of the same ceramic could follow a higher curve, BB. At present, maximum performance (highest position of Curve BB) has not been determined. It is known that if damage is not suppressed and performance follows Curves A or B, the late-time performance of most ceramics lies within a narrow range of resistance values. It is this late-time performance which is often used to rank the ballistic capability of ceramics.

Target performance depends on damage to the ceramic component. Although this damage is influenced by characteristics of the ceramic, it is strongly dependent on response of the total target system. Ceramics, in general, are strong in compression but weak in tension. Although high-quality ceramics may respond elastically to compressive stresses above 15 GPa in uniaxial strain, they may fail at tensile stresses below 0.5 GPa [9, 10]. The design of targets for ballistic evaluations of ceramics or of actual armor packages should *minimize conditions which produce damage* and provide an environment in which the compressive strength of the ceramic may be exploited for ballistic protection. The damage produced by a long-rod penetrator is found to depend on many aspects of target design and response. Current information about target behavior and sources of damage is

briefly summarized in the following paragraphs.

Impact Damage Tests with and without a steel plate in front of the ceramic reveal a large difference in the resistance to penetration, especially at early times after impact. A cover plate is believed to offer two benefits. First, it prevents the ceramic from experiencing the peak stress which may be 40 to 50 GPa during direct impact by a high-density penetrator traveling at current ordnance velocities. Second, a steel cover plate provides confinement which retards the displacement of ceramic material, as a block, from the front of the target; it also suppresses an almost explosive failure which would occur if the highest stresses were relieved at a free boundary of the ceramic.

Confinement Structural support must also be provided at the back and side of a ceramic. When a long-rod penetrator arrives at the ceramic, radial cracks quickly develop, producing wedge-shaped blocks which load the side confinement. Weakly constructed confinement may fail catastrophically. With more substantial confinement, the surrounding ductile material is engraved by each wedge. Collectively, the radial motion of the wedge-shaped blocks increases the total cross-sectional area of the target occupied by the ceramic. Even with what may be referred to as heavy confinement, the ceramic cross-sectional area may increase by several times the cross-sectional area of the penetrator. Consequently, the interaction of the penetrator's lateral surface with the penetration "tunnel" produced in the target may be much weaker than it would be if radial displacement of the wedges did not occur. As an example, Figure 4 shows the increase in area determined during penetration into a target used for ballistic evaluations. Penetration through the steel cover was complete at time T1 and penetration reached the steel backing at time T2. By time T2 the total cross-sectional area occupied by the ceramic had increased by nearly 11 times the cross-sectional area of the penetrator. Extrapolation to the abscissa suggested an early development of ceramic wedges. Deviation of the actual curve indicated confinement motion resulting from arrival of the impact shock. Internal stresses also act during penetration to displace confinement at the front and back of the ceramic. The cover plate tends to bulge outward and interfaces of a layered target tend to separate, even if the deformation of clamping structures remains within the elastic range. If interfaces extend directly to the side boundary of the target, erosion products from the penetrator and small particles of ceramic are vented to the exterior.

Wave Propagation and Interaction Most efforts to confine the ceramic component tend to consider structural support while neglecting wave propagation in the finite target. A number of factors influence wave propagation and interaction.

1. A low-impedance bonding layer is usually present between ceramic tiles and between the ceramic and its confinement. This layer is a source of tensile release and associated damage to the ceramic. Thickness of the interface layer

may not be well controlled, and air may be entrapped, further contributing to variable damage and performance.

2. Even if the interface and confinement could be perfectly matched to the acoustic impedance of the ceramic, confinement thicknesses are usually finite and tensile reflections soon return from the free boundary. Wave reflections within the ceramic then depend on the geometry of the reflecting free boundary. Tests have shown that the damage and loss of performance caused by the interaction of high-amplitude reflected waves can be reduced by installing wave (momentum) traps at the boundary of the confinement. Figure 5 shows orthogonal post-test radiographs which depict planar failure produced by interacting tensile waves reflected from the boundary of a square target. Figure 6 shows orthogonal post-test radiographs which confirm that the penetration path regains symmetry when wave traps are added at the free boundary of a square target. Figure 7 shows fully developed orthogonal failure planes revealed when the steel cover plate was removed from a square target without wave traps. This figure also shows the wedge-shaped blocks through which force at the penetration front is transmitted to the side confinement.

3. Test results suggest that low-amplitude reflected waves may contribute to the long-term cumulative damage in a ceramic target, although this is not well established. Wave traps lose effectiveness as the wave amplitude decreases, so the reflection and interaction of weak stress waves is not easily controlled.

Resistance to Penetration Many aspects of design and behavior are believed to influence the resistance of a ceramic target to penetration by a long rod. Cover plates are necessary to prevent severe impact damage to the ceramic, but relatively slow penetration through the cover plate allows time for the faster impact shock to damage the ceramic before the penetrator arrives. Damage by intersecting tensile waves from a square target boundary, and the resulting degradation of performance, were noted earlier. Converging tensile reflections from a circular target boundary may cause a greater decrease in the resistance to penetration. When the penetrator arrives at ceramic under a cover plate, it commonly finds a material which still is highly resistant to penetration. The erosion rate increases and erosion products commonly flow into the interface between the cover plate and the ceramic. The cover plate bulges to accommodate the erosion products, while the ceramic experiences a compressive stress which may suppress damage and increase the resistance to penetration. Frequently, target construction allows separation of the entire interface, allowing a lateral flow of erosion products and failed ceramic directly to the outside of the target, relieving internal stresses. This

behavior may promote damage and reduce the resistance of the ceramic to penetration. As penetration proceeds into the ceramic, major failure planes develop, freeing blocks of ceramic through which forces at the penetration front are coupled to the confinement. At the side of the penetration path, radial cracks produce pie blocks which are forced against the side confinement. As noted before, the increase in area at the boundary can be many time the cross-sectional area of the penetrator. This may influence granular flow in the penetration path, but it also may provide an alternative means for displacing ceramic from in front of the penetrator. Major failure planes, intersecting the penetration axis, further improve the coupling to confinement at the front and back of the ceramic. This must contribute to deformation, separation of interfaces, additional loss of ceramic from the target, and a further decrease in resistance to penetration. Sequential failure of the confinement may make a greater contribution to cumulative damage than long-term wave interactions. Experimental studies may soon provide an answer.

Summary It is clear that the mechanics of penetration for an armor containing ceramic elements is very different from the purely metallic case. The concept of *intrinsic* resistance is, for ceramic elements, almost completely spurious. It has become evident that, due to the mechanisms just discussed, the penetration resistance of a ceramic target depends fundamentally on the response of the total target system. Current studies at the BRL show that modified target configurations can produce a significant increase in the resistance to penetration, but the full potential for improvement has not yet been determined. Current ballistic tests clearly *do not* provide an environment in which the constitutive response of an individual ceramic material has a major influence. Indeed, a crucial challenge in the analysis of ceramic armors is to understand the basic penetration mechanics well enough so that armor packages may be designed which *do* exploit the behaviors of different ceramics. It is further apparent that to obtain reliable predictions of ballistic performance, computational simulations must employ more accurate modeling of dynamic material behavior than is now the case and must treat the response of the total target system. Substantial progress will proceed from accurate simulation of carefully controlled experiments.

1.3 Phenomenological Observations of Penetration Involving Ductile Materials (L. Magness, M. Raftenberg, J. Walter)

While the hydrodynamic picture of ballistic penetration (Figure 1) is appealing both for its simplicity and successes, it ignores an *essential* aspect of the solid state: internal structure. In mechanical terms the internal structure (microstructure) of solids is expressed as material *anisotropy* and *inhomogeneity*.[2] It has

[2]Bulk specimens of metals are usually aggregates composed of many crystals which are always anisotropic and may be individually inhomogeneous due to second phases, inclusions, etc. The

long been known that at the *intra*granular scale, plastic flow of crystalline solids is a very anisotropic and inhomogeneous process. Under continued deformation, microscale inhomogeneities may grow in extent and so develop into macroscale failure mechanisms such as ductile rupture (growth and coalescence of voids) or erosion/fragmentation by adiabatic shear bands. In addition, the microscale processes which occur during plastic flow can produce macroscopic *strain softening* behavior. When this occurs shear flow localization (shear bands) may be initiated by geometric stress concentrations independent of material inhomogeneity. While both ductile voids and shear bands are important failure modes in ballistic impact we focus primarily on the latter in our discussion here.

Adiabatic shear localization has received increasing attention in recent years as it is a principal mode of deformation and failure in a variety of ductile materials at moderate-to-high rates of deformation. The basic mechanism for adiabatic localization is an *autocatalytic* process of local heating (due to plastic work) accompanied by thermal softening which, if strong enough to overcome strain or strain rate hardening, causes an increase in the local rate of plastic work and so intensifies the heating. While recognition of thermal softening as a localization mechanism dates back to Tresca [11] (see Johnson [12]) and more recently to Zener and Hollomon [13], it is only during the last ten to fifteen years that there has been a fairly steady effort to analyze and model this phenomenon. It is worth noting that the phrase "adiabatic shear" is an historic misnomer since local heat conduction is actually an essential aspect of the micromechanics of this phenomenon!

During a ballistic impact adiabatic shear bands may occur in either an *isolated* or a *distributed* mode. Isolated shear bands tend to occur when the macroscopic geometry of the target and penetrator afford a sufficiently strong concentration of shear stress and strain rate, but the overall deformation rate (impact velocity) is not so large as to cause distributed shear band nucleation from micromechanical defects. The most striking example of this mode is the formation of a *plug* in a monolithic target plate when struck by a blunt-nosed rod [14]. Once the plug boundary (a macroscopic shear band) begins to form it propagates rapidly and, under continued loading, will reach the rear surface of the plate. Although the material inside the thin plug boundary[3] is severely deformed it is also thermally softened so that *far* less energy is needed to propagate the plug boundary than would be required for the penetrator to advance by causing gross plastic flow in the target. Consequently, when plugging occurs the armor plate will display much lower resistance to penetration than would be predicted by a hydrodynamic penetration model which accounts only for the relative mass densities and yield strengths of the target and penetrator materials. Post-mortem examination of

interfaces between adjacent crystals are another inhomogeneity in such a material.

[3]In a high-strength steel the plug boundary may be less than ten microns thick.

deep penetration tunnels in high-strength steel monoliths reveals shear bands that emanate away from the tunnel in a spiral pattern. The visible bands are the trace in the section plane of two families of (apparently) counter-winding, helical, shear surfaces which intersect to produce pyramidal fragments. Often, a tube composed of these fragments (welded together because of the high temperatures which occur during formation of the shear bands) surrounds the penetrator tunnel, which has a roughened wall due to ejection of some of the fragments. Neither feature appears in targets of lower strength steel.

As suggested above, distributed shear banding tends to occur at higher impact speeds and in regions (e.g. near the target-penetrator interface) where the macroscopic rate of deformation is large enough to initiate band growth from preexisting or deformation-induced material inhomogeneities. Although not as obvious as plug-boundary formation, distributed shear band formation is no less important for the penetration process. In this mode large numbers of bands nucleate in a more or less dense distribution within a region of material. As the bands grow the material's macroscopic strength is reduced anisotropically because the bands tend to be oriented in the local directions of maximum shear stress or shear strain rate. Here again the target presumably offers less resistance to the incoming penetrator than it would if shear bands had not formed. Ultimately, the distributed shear bands may coalesce to form fragments of the target material. Upon perforation, these fragments may comprise most of the behind-armor debris which is one of the principal lethal mechanisms of the penetrator. Experimental results of Curran *et al.* [15, 16, 17] indicate that adiabatic shear banding is the *dominant* mode of plugging, erosion and fragmentation in impacts of 4340 steel or depleted uranium (DU) rods on rolled homogeneous armor (RHA) plates over a range of velocities from below to well above the ballistic limit. Thus, in order to estimate the distribution of fragment sizes and velocities (an important capability for terminal effects codes) it is essential that models be based on the actual damage processes leading to fragmentation.

1.3.1 Observations of Shaped-Charge Jet Penetration into Steel Armor

Shear banding is always observed in rolled homogeneous armor (RHA) target material following perforation by a shaped-charge jet. Figure 8 is an SEM micrograph showing a shear band in a 12.7 mm-thick RHA plate that has been perforated by a jet from a shaped charge warhead. The warhead was fired at a standoff of 12 charge diameters[4](CD) and the jet tip speed was 7.7 km/s prior to impact. This band has been exposed by a diametral section through the perforation hole. It emanates from that hole's boundary. Three issues suggested by this and other

[4]Throughout this subsection one charge diameter is 81.3 mm.

experiments conducted at BRL will be discussed: structure within the band; the occurrence of a reproducible, characteristic shear band geometry; and the occurrence of cracks and/or voids within the band.

Structure Within a Shear Band in Steel Armor At the magnification of Figure 8, no structure is apparent inside the shear band. This is in contrast to the surrounding material which still exhibits the lath structure characteristic of the original martensite. (Note however, that these laths clearly have been rotated in the surrounding material, and have become roughly aligned with the shear bands.) Rogers and Shastry called white-etching bands, such as that of Figure 8, "transformed shear bands", implying a phase transformation that they postulated to have occurred, involving austenitization and subsequent quenching [18]. They supported this hypothesis with measurements of increased microhardness within the band. In a recent work, Beatty *et al.* [19], presented Selected Area Diffraction Patterns (SADP) within bands and in the surrounding martensite in 4340 steel. The diffraction pattern was found to vary gradually with distance from the center of the shear band, with no clear discontinuity occurring at the band's periphery. This and their inability to find remaining austenite within the bands casts some doubt on the assumption of phase transformation. The identity of the structure within a shear band and the role of phase transformation in the genesis of the band seem to be unresolved at present.

Shear Band Geometry in Steel Armor Our knowledge of the range of geometrical complexity that shear bands can exhibit is very limited. Three-dimensional mappings of shear bands in target material would be useful at this time. The single cross-sectional view of a shear band in Figure 8 has two obvious geometric features: a fairly uniform 6 μm width and the existence of little curvature. These two observations have some general validity in that they have been found applicable to other shear bands emanating from the target hole and exposed by other radial cuts in this same experiment. However, geometries of shear bands that formed radially closer to the shot line are difficult to determine in such a ballistic test. The loading history in the steel during its penetration varied with position, and it is quite possible that any characteristic features of shear band geometry could have varied correspondingly.

One approach to the question of the sensitivity of shear band geometry to the ambient stress environment during ballistic penetration is to recover fragments from ballistic tests. Figures 9 and 10 are photomicrographs which display a single RHA fragment recovered from a second test involving perforation of a 12.7-mm-thick plate by a copper jet. Here the shaped charge warhead was fired at a shorter standoff of 3 CD. The target plate hole's final diameter is 14 mm, the same as in the first test at the longer standoff. Thus the fragment in Figures 9 and 10 indicates the condition of steel radially closer to the shot line than that of Figure 8. Figure 9 shows the shear band still to be straight, but Figure 10 shows its width to be 20 to 30 μm. This width is larger than that of the shear band in Figure

8 by a factor of 3 to 5. Figure 11 shows a photomicrograph of another RHA fragment from this test involving perforation by a shaped-charge fired at 12 CD standoff. This fragment's boundary is seen to be lined by a white-etching region of perhaps 25 to 100 μm width, that bears little geometrical resemblance to the shear band of Figure 8. However, the comparison is marred by the fact that the fragment of Figures 9 and 10 perforated one or more sheets of mild steel before coming to rest in the witness pack used for its recovery. This points up the need to develop a non-destructive fragment recovery technique for use in these ballistic tests. A desirable but difficult-to-achieve feature of such a technique would be the preservation of information regarding each fragment's original location on the target plate.

A second approach to examining the question of the dependence of shear band geometry on original location in the target plate is through laboratory experiments. As a promising example, reference [19] documents the application of a split Hopkinson bar technique to a "hat-shaped" specimen of RHA. Laboratory techniques such as this offer a distinct advantage over ballistic penetration tests in that in the former, loading conditions within the specimen can be relatively well characterized. However, if the ultimate goal is to illuminate phenomena pertaining to shear bands that occur in ballistic penetration, then the loading conditions produced in a laboratory experiment should be similar to those occurring at some location of interest in a target. As a check, shear bands produced in the laboratory should be shown to resemble those displayed in micrographs from ballistic tests.

Shear Band Association with Cracks and Voids in Steel Armor The ability to predict information on fragments produced by a given penetrator-target interaction is a current challenge of great practical importance. In this regard, more knowledge of the micromechanical processes leading to fragmentation is needed. Micrographs such as that of Figure 12 seem to implicate shear bands. This shows a shear band in the same target plate considered in Figure 8. A crack clearly extends along part of the shear band's length. Figure 13 shows the same shear band and crack at smaller magnification. The crack is seen to begin at the hole boundary; the process of fragment formation has apparently been caught in a state of partial completion. The sequence of events linking shear band localization to macroscopic cracking is still unclear. Perhaps the increased microhardness within the band provides a clue.

Spheroidal voids are shown in the same target plate in Figure 14. These have coalesced to form a crack, along which the martensitic laths have become aligned. Such voids may constitute a second micromechanical mechanism for fragmentation. However, it is not yet clear to what extent they are indeed a separate mechanism, independent of shear banding.

1.3.2 Comparison of Uranium Alloys and Tungsten Composities as Long Rod Penetrator Materials

The importance of both plastic inhomogeneities and material anisotropies to the process of penetration is also illustrated by a comparison of the observed phenomenology and resulting ballistic performance of uranium alloy, tungsten heavy alloy composite, and tungsten single crystal penetrators.

Depleted uranium (DU) alloys and tungsten heavy alloys (WHA) offer both the high material densities (for penetration performance) and useful mechanical properties (needed for the integration of the penetrator core in engineered kinetic energy (KE) long rod projectiles and cartridge assemblies). Metallurgically, however, DU and WHA are very different kinds of materials.

The DU materials are true alloys. The standard DU-3/4Ti alloy can be cast and heat-treated in much the same way as iron-carbon (steel) alloys, Eckelmeyer [20]. In contrast, Tungsten is a refractory metal and pure tungsten products generally have poor ductilities and toughnesses, and require very high processing temperatures. Therefore the WHAs used for KE penetrator applications are actually composites of tungsten particles in a ductile metal matrix (usually consisting primarily of nickel and iron), and usually produced by liquid-phase sintering techniques. The density of the WHA composite depends on its tungsten content, and the mechanical properties depend on both its tungsten content (percentage of ductile metal matrix) and on its processing history, Gurwell *et al.* [21]. Because DU and WHA are so very different metallurgically, they also differ significantly in many fundamental mechanical, thermal, etc. properties.

The ballistic performances of DU and WHA projectiles also differ by a small, but significant, amount. Penetrators of the standard DU-3/4Ti alloy consistently require lower impact velocities (by approximately 100 m/s)[5] to defeat thick steel and steel/ceramic laminate targets than WHA projectiles of equal mass and identical geometry (i.e. equal density) Magness and Farrand [22].

Examinations of residual DU and WHA penetrators embedded in steel armor (Figures 15 and 16, respectively) reveal that the two materials display very different deformation behaviors during the penetration process. In the case of the WHA penetrator (Figure 16), the relatively smooth erosion and back-extrusion of the material at the penetrator's head is qualitatively consistent with the fluid-dynamic idealization of penetration depicted in Figure 1. The WHA material undergoes a great deal of plastic deformation as it approaches and is inverted at the penetrator-target interface. A large mushroomed head is found on the residual penetrator embedded in the target (Figure 16) and is routinely observed on residual WHA penetrators after exiting finite steel targets (Figure 17). The evolution of the WHA microstructure in Figure 16, from the originally spherical tungsten

[5]This relatively small velocity difference translates into a significant difference ($\approx$ 2 km) in the effective range of such projectiles by virtue of air drag effects.

particles to highly elongated stringers, provides further evidence of the large plastic strains that occur as the material is inverted. On closer examination, of course, the flow of the penetrator material does differ from fluid behavior. Because the WHA is a solid, small elastic strains and some small plastic strains manage to propagate away from the interface. The "flaring" of the residual rod as it feeds into the mushroomed head is evidence of this. Another significant departure from the fluid-dynamic ideal is the development of plastic localizations, or small regions of larger than average plastic strains, near the periphery of the mushroom. The eventual discard of material from the periphery of the mushroomed head ultimately occurs along some of these localizations.

The deformation of the DU-3/4Ti penetrator has a very different appearance (Figure 15). Localizations of the plastic deformation develop very quickly along planes of highest local shear stress and at relatively small values of strain. The subsequent discard of the back-extruding material along these shear planes occurs before a large mushroomed head can develop on the penetrator. As a result, the residual DU penetrators observed exiting the rear face of finite steel targets lack the large mushroomed head of the WHA penetrators. Instead, they display a pointed nose (Figure 18), shaped by the chiseling action of the local shear failures occurring during the penetration process. It is the ability of the DU alloy penetrators prevent the build-up of a large mushroomed head which is ultimately responsible for their superior ballistic performance.

A comparison of the penetration cavities formed by DU and WHA projectiles penetrating into thick steel blocks is shown in Figure 19. The hole profiles in Figure 19 reveal that, during much of the penetration process, the DU penetrator creates a smaller diameter penetration tunnel. Therefore, less of the kinetic energy of the DU projectile is expended laterally, to displace a larger *diameter* hole into the target, and more of its kinetic energy is available to penetrate to a greater *depth* in the thick target. Against lesser thicknesses of armor plate, which both the DU and WHA projectiles are able to perforate, the DU penetrator does so more efficiently and therefore has a lower ballistic limit.[6]

The distinct deformation behaviors exhibited by the DU and WHA penetrators are a result of differences in their *thermo*mechanical properties. Under the very high strain rate loading conditions of the penetration process, there is essentially no time for the macroscopic transport of the heat being generated by the deformation of the penetrator. The thermal-softening induced by this adiabatic heating overcomes the usual strain-hardening and strain-rate hardening much more quickly in the DU than in the WHA. The result is a net *strain-softening* behavior in the DU, under which small perturbations in the plastic strain or temperature fields can quickly grow into the plastic localizations (adiabatic shear bands) ob-

[6]For a given penetrator and target, the *ballistic limit* is defined to be the lowest penetrator velocity which will produce perforation.

served in the DU residual penetrators. As evidenced by the smoothly deformed microstructures and the large mushroomed heads which develop on the WHA penetrators, the plastic deformation is much more stable in this material.

A related, but distinctly different, illustration of the role of the penetrator material's behavior on penetration performance is the comparison of the behavior and performance of different orientations of tungsten monocrystal penetrators and polycrystalline pure tungsten penetrators. Due to the thermomechanical properties of pure tungsten (high strain rate sensitivity, relatively low rate of thermal softening, etc.), the plastic deformation of the tungsten polycrystal penetrator is extremely stable (Figure 20). In fact, the "mushrooming" of the tungsten polycrystal is more extensive than that of the WHA resulting in poorer ballistic performance than a WHA penetrator of equivalent mass and geometry, Magness [22]. However, ballistic tests show that the performance of monocrystalline tungsten penetrators (Bruchey, Horwath and Kingman [23]) vary with their crystallographic orientations. In one case, with the axis of the penetrator parallel to the <110> direction in the lattice, the mushrooming can be even more exaggerated than in the pure tungsten polycrystal (Figure 21). As a result, the diameter of the penetration cavity is considerably larger and the projectile achieves very low depths of penetration. In contrast, if the axis of the rod is parallel to the <100> axis of the crystal, cleavage failures appear in the head of the penetrator after only small plastic strains (Figure 22) and the deformed material is more quickly discarded. The <100> oriented crystal penetrator creates a much smaller diameter penetration tunnel and delivers penetration performance approximating that of DU. In this case, anisotropies in the strengths and flow behaviors, rather than plastic flow localization, lead to the very different modes of deformation and ballistic performances exhibited by the monocrystalline tungsten penetrators.

The differing behaviors and ballistic performances of DU, WHA, and single crystal tungsten projectiles serve as excellent tests of the ability of ballistic impact simulation codes to accurately represent the response of penetrator and armor materials during the penetration event. Conversely, the incorporation into simulation codes of state-of-the-art material models and algorithms should become a central goal for the code development community.

1.3.3 Conclusions

The fundamental reason for non-hydrodynamic behavior in the penetration of metallic targets is the complex internal microstructure of metals and its manifestations as macroscopic strength and localized deformation modes which lead to material failure. The occurrence of ductile failure modes depends strongly on several aspects of the ballistic impact.

1. The macroscopic thermo-visco-plastic (TVP) response of the material.

2. Features of the material microstructure which can serve as nucleation sites for shear band or voids.

3. Features of the macroscopic loading (e.g. hydrodynamic pressure/tension, stress concentrations, etc.) which can encourage or supress localized deformation.

The macroscopic TVP response of high strength steels is quite favorable for shear band formation and in this context some aspects of band morphology and metallurgy were discussed in section 1.3.1. Most notable is the *severity* of the localization in a shear band and the fact that bands may serve as nucleators for other failure mechanisms e.g. cracks. Lastly, section 1.3.2 emphasized the degree to which a material's shear band *susceptibility* is affected by its TVP response. Moreover, the relative shear band susceptibility of different materials produced markedly different penetration performance.

2 Terminal Effects Codes (K. Kimsey, G. Randers-Pehrson)

Computer codes used to study the armor penetration process are usually known as "hydrocodes", or more accurately, "wave propagation codes". Wave propagation codes fall into two classes: Eulerian and Lagrangian (a third class, Arbitrary Lagrangian Eulerian, is currently emerging). Eulerian codes used at BRL include HULL [24], MESA [25], and CTH [26]. Lagrangian codes used at BRL include DYNA2D/3D [27] and EPIC2D/3D [28] and some of their derivatives. CTH and MESA are now being evaluated for modeling armor/anti-armor problems.

In either approach, the problem is divided into a large number of small computational cells or elements. The solution to the problem proceeds over small time steps, typically a tenth or hundredth of a microsecond. At each time step the stress state within each computational cell is determined from the deformation of the cell together with the equation of state (pressure-volume relationship) and constitutive model (describing the thermo-visco-plastic response) of the material that it contains. From the stress state, the equation of motion is used to determine the deformation to be used as input to the next time step. The Lagrangian and Eulerian approaches differ in the treatment of material motion. In the Lagrangian codes, the cell's mass is assigned to the nodes at the cell corners, and the nodes move through space according to the equation of motion. The Lagrangian cell becomes deformed and moves along with its corner nodes. In the Eulerian approach, the cell does not move, but material from neighboring cells flows in or out according to the equation of motion. All of the Eulerian codes use a two-step solution scheme. The first step is a Lagrangian step in which the cells distort to

follow material motion. The second step is a remesh step where distorted cells are mapped back, i.e. advected, to the Eulerian mesh.

Because of the severe deformations which occur in the penetration process, Lagrangian codes generally cannot treat such problems unless special measures are taken. In EPIC and DYNA, "eroding sliding interfaces" are used, wherein severely deformed cells are removed from the computation according to criteria such as accumulated plastic strain. Such special treatments extend the utility of Lagrangian codes for modeling deep penetration problems. Eulerian codes can model severe deformation more readily, without resorting to special treatments, but they too have disadvantages, for example difficulties in advecting material stress histories. Eulerian codes generally require much larger amounts of computer memory and processor time.

Most armor/anti-armor problems are inherently three-dimensional. Some two-dimensional problems such as normal impact and penetration of semi-infinite armor are useful, however, mainly for validation of the codes. Following are brief descriptions of several three-dimensional wave propagation codes in current use for penetration mechanics studies at BRL.

HULL is a family of computer programs for solving continuum dynamics problems. The code solves the finite difference analogs of the governing partial differential equations for two- and three-dimensional Eulerian and Lagrangian formulated problems as well as coupled Eulerian/Lagrangian solutions. Material advection is based on a first-order donor-cell algorithm with a heuristic multimaterial diffusion limiter to preserve material interfaces. Most solids in HULL are modeled with the Mie-Gruneisen equation of state. Concrete, geological materials and explosive products equations of state are also available. Material failure models include maximum principal stress, maximum principal strain,and the Hancock-Mackenzie triaxial failure model. Plasticity models include elastic-perfectly plastic with provisions for work hardening and thermal softening.

MESA is a new 3D Eulerian code which is being developed for armor/anti-armor work by a team at Los Alamos National Laboratory. This code was written to take advantage of new high-order accurate advection algorithms and interface reconstruction methods. Plasticity models in MESA include the Johnson-Cook and Steinberg-Cochran-Guinan-Lund models, and various simpler ones. The ductile fracture model TEPLA-F [29] has also been incorporated in MESA.

CTH is Sandia's new Eulerian code. Like MESA, it incorporates new high-order accurate algorithms. It has its roots in the previous Sandia code, CSQ. CTH solves the finite difference analogs of the governing conservation equations using an Eulerian solution scheme. CTH models solid dynamics problems involving shock wave propagation, multiple materials and large deformations in one, two and three dimensions. CTH models elastic-plastic behavior, high explosive detonation, fracture and motion of fragments smaller than a computational cell. Plasticity models include elastic-perfectly plastic with thermal softening, Johnson-

Cook, Zerilli-Armstrong and Steinberg-Guinan-Lund. The Johnson-Holmquist [30] brittle material model has also been incorporated in CTH. Both analytical (Mie-Gruneisen) and tabular equations of state are available for modeling the hydrodynamic behavior of materials. Three types of high explosive burn model are available; programmed burn, CJ volume burn and history variable reactive burn. The Jones-Wilkins-Lee equation of state is available for modeling detonation products. Fracture initiation is based on maximum pressure and principal stress.

DYNA3D is a Lagrangian explicit finite element code for analyzing the transient dynamic response of three-dimensional solids and structures. A product of the Lawrence Livermore National Laboratory, it has a wide variety of element types and material models and sophisticated treatment of contact/impact interfaces. A version of the code supported by Dr. John Hallquist, the original author of the code and now an independent consultant, incorporates an automatic eroding interface algorithm. Recently, researchers at LLNL have implemented a slideline adaptive node definition (SAND), i.e. eroding slidelines, algorithm into LLNL's DYNA3D code.

EPIC is a Lagrangian explicit finite element code written by Dr. Gordon Johnson of Alliant Tech Systems (formerly a division of Honeywell). It incorporates an eroding surface capability, and uses primarily Johnson's material models (Johnson-Cook for metals, Johnson-Holmquist for ceramics, and the JWL equation of state for detonation products). The code uses triangular or tetrahedral finite elements rather than quadrilateral or brick-shaped ones, and consequently can frequently run problems with large deformations more readily than other Lagrangian codes.

ALE (Arbitrary Lagrangian Eulerian) codes under development include the 2D CALE code, written in the C programing language at Livermore, and a 3D mixed-zone code being developed by Livermore. The latter code is written in Fortran and has its roots in the DYNA3D code. Like DYNA3D, it has a wide variety of plasticity models, including Johnson-Cook, Steinberg- Cochran-Guinan-Lund, power law hardening, crushable foam, geologic models, and various orthotropic models. Sandia is also working on a 3D ALE code called RHALE.

In this article, we focus on the material modeling and equation of state modeling in present day terminal ballistics codes. The predictive capability of current wave propagation codes for impact studies is dependent on the material model and properties that are used in the simulations. Metals, until recently, were the materials of primary interest. It is common in existing wave propagation codes for impact studies to divide the deformation behavior of metals into volumetric and deviatoric parts as

$$\sigma_{ij} = -p\delta_{ij} + s_{ij}\,, \tag{2}$$

in which σ is the stress tensor, s is its deviatoric part and p is the pressure. The

volumetric behavior is obtained from an equation of state which describes the interdependence of thermodynamic properties, such as pressure, energy, density and temperature. For impacts where the striking velocity is below the sonic velocity, some variant of the Mie-Gruneisen equation of state is commonly used. Beyond this range (hypervelocity impact) the Tillotson equation of state is favored. Some codes also use tabular equations of state to represent equation of state surfaces of arbitrary complexity which are valid for a wide range of densities and temperatures. Examples of tabular equations of state include SESAME (Bennett *et al.* [31], Kerley [32]) and ANEOS (Thompson, [33]). Explosive detonation products are most commonly represented by the well-known JWL analytical equation of state. A desirable feature of the analytical equation-of-state models is that they are easy to use and, for most metals, model parameters can be obtained from the literature (van Thiel [34]; Marsh [35]; Kohn [36]; Steinberg [37]; Dobratz and Crawford [38]).

An incremental elastic-plastic formulation is used to describe the deviatoric response of metals in present finite difference and finite element codes. Most follow the description first given by Wilkins [39, 40]. The plasticity descriptions are usually based on the assumed decomposition of the strain rate tensor into elastic and plastic parts

$$\dot{\epsilon}_{ij} = \dot{\epsilon}^e_{ij} + \dot{\epsilon}^p_{ij}\,, \tag{3}$$

together with incompressibility of the plastic part

$$\sum_i \dot{\epsilon}^p_{ii} = 0\,. \tag{4}$$

The von Mises yield criterion is commonly used to determine if a material element is undergoing plastic flow.

Traditionally, the plasticity models in wave propagation codes for impact studies have been relatively simple, of the elastic, perfectly-plastic type, and have been implemented using the radial return algorithm formulated by Wilkins [39, 40]. More recently viscoplastic models have been implemented in wave propagation codes to represent the dependence of the flow stress on strain, strain rate, pressure, temperature or some combination thereof. Viscoplastic models for metals include those of Johnson and Cook [41] and Zerilli and Armstrong [42].

The Johnson-Cook model for the von Mises equivalent flow stress is expressed as

$$\sigma_f = [A + B(\epsilon^p)^n]\left[1 + C\ln\left(\frac{\dot{\epsilon}^p}{1.0\mathrm{s}^{-1}}\right)\right][1 - (T^*)^m]\,, \tag{5}$$

where σ_f is the flow stress, ϵ^p is the equivalent plastic strain, $\dot{\epsilon}^p$ is the rate of change of the latter, and T^* is the homologous temperature; A, B, n, C and m are constants. The expression in the first pair of brackets represents the dependence of the flow stress on (von Mises) equivalent strain. The expressions in the

second and third brackets represent the dependence on strain rate and temperature, respectively. The model is based on a numerical fit to torsion and tension test data at ambient and elevated temperatures. Use of the model outside the range of the test data may not be warranted. Model parameters for a number of metals are given by Johnson and Cook [41] and Johnson and Holmquist [43]. The Johnson-Cook model has been implemented in the EPIC, DYNA, CTH and MESA codes.

Figure 23 compares computed semi-infinite penetration depths with quarter-scale test data, Magness [44], for 65 gram, L/D 10, depleted-uranium alloy (U-3/4Ti) and tungsten heavy alloy (WHA) rods impacting semi-infinite RHA targets at striking velocities between 800 and 1800 m/s. The solid symbols represent CTH results using the Johnson-Cook model to describe the flow stress for both rod and target materials. The CTH results compare well with the test data and also reflect the observed gap in performance between these two materials. Magness and Farrand [22] conducted ballistic tests and microstructural analyses of the performance of uranium and tungsten heavy alloys and identified the strain-softening behavior developed by the uranium alloys under high rate loading and the resulting thermo-mechanical (adiabatic shear) instability, as the mechanism responsible for uranium's superior performance. It is interesting to note that while the Johnson-Cook model does not explicitly model adiabatic shear bands, it appears to capture some aspects of the "global" behavior of the two alloys under impact loading (for the striking velocities studied).

Zerilli and Armstrong [42] have shown an improved description of copper and iron cylinder impact (Taylor) test results using their dislocation-mechanics-based constitutive relations for body centered cubic (bcc) and face centered cubic (fcc) materials. The Zerilli-Armstrong model is based on the observation that each material structure type (fcc, bcc, hcp) will have its own constitutive behavior, dependent on the dislocation characteristics for a particular structure. Thus, separate relations are required to describe flow stress for bcc and fcc metals. For OFHC copper (fcc), the flow stress is given by

$$\sigma = \Delta\sigma_G' + c_2\epsilon^{1/2}\exp[(-c_3 + c_4 \ln \dot{\epsilon})T] + k\ell^{-1/2}, \tag{6}$$

whereas for Armco iron (bcc) the flow stress is given by

$$\sigma = \Delta\sigma_G' + c_1\exp[(-c_3 + c_4 \ln \dot{\epsilon})T] + c_5\epsilon^n + k\ell^{-1/2}; \tag{7}$$

the constitutive variables have the same interpretation as in (5) except that ℓ is the grain size. Values for the eight material constants: $c_1, \ldots, c_5$, $\Delta\sigma_G'$, k, n, for OFHC copper and Armco iron are reported by Zerilli and Armstrong [42]; this model is currently available in EPIC, CTH and MESA.

The Mechanical Threshold Stress, Follansbee [45], and the Steinberg-Cochran-Guinan-Lund, Steinberg *et al.* [46, 47], material models relate the macroscopic

stress-strain behavior to microscopic properties. Material parameters have been published for the latter model for seven metals: beryllium, molybdenum, niobium, niobium alloy fansteel 85, tantalum, tungsten, vanadium, and for some other materials (Steinberg [37]). Both models have been implemented in MESA.

Computational failure models for impact loading situations are discussed in review articles by Seaman [48] and Zukas [49] and the NMAB Committee report on Materials Response to Ultra-High Loading Rates [1]. Briefly, empirical failure models of varying degrees of complexity exist. Some have been applied successfully in high velocity impact simulations. For the most part, though, failure criteria and models are of an ad-hoc nature, lacking a micromechanical basis to comprehensively treat problems involving both brittle and ductile failure modes. Different criteria apply for different impact scenarios and there are at present no guidelines for analysts wishing to select a failure criterion appropriate to varying conditions.

The simplest of the failure initiation criteria are based on instantaneous values of a field variable, such as pressure, stress, strain, plastic work, or some combination thereof. Once the criterion has been satisfied at a given location, failure is considered to occur instantaneously. The post-failure behavior of materials can be described in a number of ways. The failed material may be removed entirely from the calculation or be described by a modified constitutive function.

Time-dependent initiation criteria represent the next level of sophistication and have been successfully applied in several situations. One of the earliest time-dependent models is attributed to Tuler and Butcher [50]. Failure is assumed to occur instantaneously only after the stress has remained above a threshold stress level for some length of time, below which no significant damage will occur regardless of duration.

Criteria in which damage accumulation is a function of field variables have been developed by Davison [51] and Johnson [52] In these models the rate of damage accumulation is taken to be a function of strain, temperature, pressure, strain rate and current damage level. Damage levels are used to degrade a materials' characteristics and sometimes trigger instantaneous failure.

Researchers at SRI International (Seaman and Shockey [53], Seaman *et al.* [54] and Erlich [55]) have been developing "microstatistical" failure models. Ductile failure damage is initiated when the average stress exceeds a tensile-pressure criterion. Brittle fracture is initiated when the maximum normal stress exceeds a tensile threshold. Shear banding begins when the maximum plastic shear strain exceeds a critical value. After initiation, voids, cracks, and shear bands nucleate and grow according to experimentally determined rate equations. These failure models have not been implemented in many production codes due the limited number of materials which have been characterized as well as the requirement to conduct extensive materials tests in order to obtain model parameters for new materials.

No definite failure model has yet emerged, nor has a library of data to drive the various models for materials of practical interest. Therefore, for want of an adequate data base for advanced failure models, most high velocity impact simulations are performed with the simplest failure models. In many cases, simple failure models produce results in agreement with experiments.

Brittle material modeling is a topic currently of great interest in the computational penetration mechanics community, primarily because of the interest in ceramics as candidate armor materials. Despite the recent surge in activity, there does not yet appear to be common agreement in the developer's community on the correct modeling approach. Nonetheless, the first models intended to address the behavior of ceramic materials under ballistic impact are becoming available to the general user community.

Probably the most notable of these new models is the Johnson-Holmquist model [30], which has been implemented in the 1990 version of the EPIC code, Johnson and Stryk [28]. The salient features of this model include Mohr-Coulomb-like behavior of the yield surface (i.e. yield strength proportional to pressure), and an equation controlling the evolution of a scalar "damage" parameter. When the damage parameter reaches a critical value, failure is modeled by imposing a pressure jump intended to account for shear-induced dilatancy believed to occur in the comminuted ceramic. However, neither the magnitude nor the onset of the pressure jump is a function of material shearing rate, as would be indicated by granular flow theory.

Each of the brittle material models which are beginning to surface in the computational penetration mechanics community address issues of ceramic response deemed important by their respective developers. The features of ceramic response which are being addressed in various forms by various developers include: volumetric bulking upon failure; shear induced dilatancy; frictional effects in failed ceramic rubble; modulus degradation; Mohr-Coulomb-like failure surfaces in ceramics; microscopic cracking and void formation; and "damage" evolution. It remains to be seen which of these model features are necessary to model the ballistic behavior of ceramic materials. Toward this end Kipp and Grady of Sandia are conducting experiments (mostly one-dimensional plate impacts) to measure the dynamic response of ceramics.

3 Finite Strain Plasticity (N. Huffington)

3.1 State of Modeling in Current Terminal Ballistics Codes

It should be understood that the theory of plasticity has not achieved a state of uniform acceptance comparable to the theory of elasticity, even for relatively small strains. Even such basic concepts as the plastic potential and use of associated

vs. non-associated flow rules are still unsettled. For the historical development of plasticity theory one may refer to Hill [56] for a condensation of results up to 1950 and to Malvern [57] for publications up to 1969. Subsequent publications (very numerous) are scattered throughout the research literature. Since large plastic strains are possible only in materials which possess considerable ductility, the discussion which follows is essentially concerned with various aspects of constitutive modeling required for representation of behavior of ductile metals (rubberlike materials are usually treated using specialized nonlinear elastic constitutive models). No attempt will be made to itemize which of these desirable features are currently available in specific codes; this information is usually available in the documentation for each code.

Work Hardening Provision for work hardening may vary from none (perfectly plastic material) to linear hardening (one hardening modulus) to nonlinear hardening: either a particular functional dependence of stress on strain is specified or tabular data on stress-strain pairs is used in conjunction with an interpolation routine. Linear hardening is usually satisfactory only over a limited strain range where the maximum strain is known in advance. For materials such as copper a nonlinear representation is essential since no portion of the stress-strain curve is linear. For other than uniaxial loading it is necessary to supplement the foregoing with the concept of an effective stress (usually the von Mises stress) which is a function of a scalar parameter, usually either the accumulated plastic strain or the plastic work. This approach leads to the concept of isotropic hardening, in which the yield surface maintains its shape while its growth in size depends on the parameter just cited. Isotropic hardening does not permit modeling of the Bauschinger effect, for which recourse may be made to the kinematic hardening concept of Prager [58] and Ziegler [59] in which the yield surface (in principal stress space) retains its initial size and shape but translates in the direction of the plastic deformation-increment vector. The coordinates of the center of the yield surface, usually termed the back stress tensor, must be determined by solution of evolution equations. Experimental evidence, Hu *et al.* [60], indicates that hardening is neither isotropic nor kinematic. Hodge [61] has discussed a combination of kinematic and isotropic hardening, the ratio being controlled by a parameter varying from zero to one; this has been incorporated in the DYNA codes. Essentially all terminal ballistics codes assume that the input uniaxial stress-strain curve (or data) is an odd function of strain (i.e. equal response in tension and compression). This can usually be made acceptable for modest strains by use of an appropriate strain measure (generally logarithmic strain). However, for finite strains this anti-symmetry is not true for many materials; it would be desirable to generalize the constitutive formulation to permit differing response in tension and compression.

Rate Effects Stress evaluation for materials which exhibit rate-dependent resistance to deformation, i.e. materials which obey an identifiable elasto-visco-

plastic constitutive function, is readily handled by conventional codes which supply the components of the rate-of-deformation tensor to the constitutive model subroutine. An example of such a function is the empirical Johnson-Cook model (see equation (5)), which contains a term in the logarithm of the dimensionless plastic strain rate. In addition to physical material rate effects, artificial viscosity terms are frequently employed in numerical simulations to eliminate discontinuities at shock fronts and to suppress the development of spurious hourglass deformation modes. Various constitutive formulations involving strain rates also employ the material time derivative of the Cauchy stress (e.g. the Prandtl-Reuss model); however this time derivative is not frame-indifferent. Consequently, a formulation involving the Cauchy stress, its time derivative, and the time derivative of an orthogonal rotation matrix was sought which would provide the desired frame-indifference. One such formulation employs the co-rotational stress rate introduced by Jaumann [62] which employs the material spin tensor (antisymmetric part of the velocity gradient) as the rate-of-rotation matrix. Although this stress rate is widely used in current hydrocodes it has been found [63, 64] to result in a spurious prediction of the stress in kinematically hardening (hypoelastic) materials at finite shear strains. The Jaumann stress rate is not unique in its capability to satisfy the frame-indifference requirement. There is an extensive literature concerning alternate stress rate formulations and "plastic spin"; in addition to those just mentioned, see papers by Green and Naghdi [65], Asaro and Rice [66], Nemat-Nasser [67], Lee [68], Dafalias [69], and Johnson and Bammann [70]. Despite the proliferation of ideas concerning this topic, this writer believes the identification of a stress rate model which can be rigorously justified and which will provide agreement with experiments remains to be accomplished.

Energy balance, Thermal Softening Most hydrocodes compute the plastic work at each cycle for use in the equation-of-state but few actually calculate the temperature field. An exception is the EPIC-2 code as modified by Johnson [71], which has an option to compute an incremental temperature change by dividing the local plastic work by the nodal mass and the specific heat. The temperature increment is added to the temperature from the previous cycle and the updated temperature is used in the Johnson-Cook [41] flow law which contains a term for modeling thermal softening. Between each "mechanical" cycle the EPIC-2 code performs a finite element heat conduction calculation to determine a new temperature distribution for use in the next cycle.

The DYNA3D code has no provision for coupled heat transfer calculations but does contain the Johnson-Cook constitutive model as Material Model 15 (consequently its use is only appropriate for adiabatic applications). However, separate heat conductions can be made using TOPAZ [72] to create files of temperatures to be read by the DYNA or NIKE codes, thus permitting thermal stress calculations to be performed.

The foregoing code capabilities involve numerous assumptions which may not

be generally valid and which could be avoided by greater complexity of the formulation. For example, it is assumed that 100% of the plastic work is converted to heat, that the effect of heating on material properties is instantaneous, and that the specific heat is a constant. The writer is not aware of any plasticity model in any code which approaches the generality of the formulation given by Green and Naghdi [65].

Anisotropic Plasticity The writer is not aware of any hydrocodes which currently provide treatment of generally anisotropic material in the plastic régime. DYNA3D contains a model for crushable honeycomb (Material Model 26) which has been used with some success. Initially isotropic materials may develop anisotropy during plastic deformation (texture hardening) but the computational model does not characterize the anisotropic parameters. The current versions of the EPIC codes do not appear to have any provision for anisotropy. It should be added that some of the hydrocode development groups around the country are working on including some aspects of plastic anisotropy in their codes, but general release to the user community has not yet occurred.

Failure Modeling There is a very extensive literature on modeling of material failure from both phenomenological and micromechanical viewpoints, but here mention will only be made of failure models implemented in currently employed codes. The most widely used failure model for metals is the empirical Johnson-Cook model [73]. This is a cumulative damage model which expresses the strain to fracture as a function of strain, strain rate, temperature, pressure, and equivalent stress. Once the fracture criterion has been satisfied the material can support no shear or tensile stresses but can sustain compressive hydrostatic pressure. The implementation of this and other phenomenological models in codes is usually supplemented with criteria based on maximum principal stress or minimum pressure, with options as to post-failure treatment of stresses. The micromechanically-based Steinberg-Cochran-Guinan-Lund material model [46, 47] also employs a damage accumulation parameter; this is used to calculate a strength-reduction factor which is applied to strength moduli and the spall strength.

3.2 Current BRL Efforts in Finite Plasticity

Joint BRL/MTL Program in Constitutive Modeling The BRL has provided computational support for interpretation of MTL quasi-static torsion tests. This support included modeling of the complete Lindholm-type specimen (which revealed a torsional buckling problem) and the development of a constrained generic strip model which greatly reduces computer run time and memory requirements. The DYNA3D code has been adapted to represent constitutive behavior of materials such as copper which exhibit extremely nonlinear stress-strain characteristics as well as the Bauschinger effect. A study of discrepancy between uniaxial and torsion test data has been completed [74]. Further computational

support for interpretation of MTL torsional Hopkinson bar data and for inelastic heating effects is planned.

BRL Extensions to Constitutive Models in Hydrocodes A new stress evaluation subroutine has been developed for the DYNA3D code which provides:

1. Choice of Green-Naghdi or Jaumann stress rate;
2. Mixed kinematic/isotropic hardening;
3. Input of tabular stress-strain data;
4. Use of a (J_2, J_3) yield function;
5. Johnson-Cook failure modeling and thermal softening.

This formulation will be exercised by application to a variety of simple applications and for interpretation of data being generated at MTL.

Externally produced constitutive and failure models are on the agenda for incorporation into the BRL DYNA3D and evaluation: the Mechanical Threshold Stress model [75], the Steinberg-Cochran-Guinan-Lund model, the Zerilli-Armstrong model [42], the latest version of Bammann's model [76, 77], and the failure models of J. Johnson [29]. The Nemat-Nasser/Chung plasticity algorithm [78] will also be studied for possible use in certain applications.

3.3 Current Activities Elsewhere

Dept. of Energy The new Eulerian codes MESA and CTH, have been developed at the DOE laboratories to take advantage of new 2nd-order accurate advection algorithms. New material models developed at the DOE labs include the Mechanical Threshold Stress (MTS) model and the Steinberg-Cochran-Guinan-Lund model. Both of these attempt to relate macroscopic stress-strain to the underlying microscopic mechanical behavior. Much of the experimental work involves observation of wave profiles in plane shock experiments. Work is being conducted at the DOE laboratories to port MESA and CTH to run on massively parallel computers including the Connection Machine and the N-Cube. Although massively parallel versions of these codes are still under development, some of them have demonstrated impressive speedups compared to current vector processing machines, when simulating armor/anti-armor problems.

URI Center at Univ. of California, San Diego An potentially important effort at the USCD-URI is contained in the papers [79, 80, 78] in which a new algorithm for stress increment evaluation during plastic loading is discussed. This algorithm takes advantage of the fact that the plastic strain increment is usually the dominant part of the total strain increment. The claimed advantage for this rather complex algorithm is that it permits use of large time steps in the

temporal integration of a simulation. However, for codes employing a conditionally convergent explicit integration scheme (as do most terminal ballistics codes) the restriction on step size necessary for numerical stability vitiates this advantage. This may suggest the need for less restrictive timestepping schemes than are currently in use.

3.4 Conclusions

Successful prediction of stress states and material failure in finite strain plasticity will require advances in many of the areas cited above, particularly in modeling of stress rates, Bauschinger effect, elastic and plastic volumetric effects, and elasto-thermo-visco-plastic coupling. Development of improved modeling in these areas must be guided by extensive new experimental techniques and results, especially for nonproportional loading, intermediate and high rate loading, plastically induced heating and thermal degradation, and anisotropic plasticity. BRL should be active in acquisition and evaluation of newly proposed constitutive models such as MTS, Steinberg-Cochran-Guinan-Lund, Bammann, and Zerilli-Armstrong plus several micromechanically-based failure models and should keep fully abreast of developments in ALE codes, other relevant advances in finite element / finite difference technology and massively parallel computing.

4 Modeling of Material Response due to Shear Band Formation (M. Raftenberg, J. Walter)

In modeling adiabatic shear band formation, two distinct aspects of the problem are apparent: shear band *nucleation* and subsequent shear band *growth*. Addressing the second aspect first, we may say for purposes of discussion that a shear band has nucleated when it has grown to a size[7], perhaps one to several grain diameters, such that its subsequent growth is governed by the macroscopic (continuum) elastic, thermal, visco-plastic response of the material and the local, macroscopic loading applied to the band. In particular, extant experimental results indicate that once nucleated, adiabatic shear bands are little affected by and often may completely obliterate any preexisting microstructure. Consequently, most attempts to model shear band growth have been within a continuum mechanics framework and have relied on phenomenological thermo-visco-plastic flow laws. For problems such as target plugging and, more generally, to explore the post-nucleation dynamics of band growth and interaction this approach is feasible and has provided important results.

[7] Like brittle cracks, adiabatic shear bands are *essentially* planar entities whose in-plane size may vary from a few to many thousands of times the band thickness.

In contrast with shear band growth, distributed shear band nucleation clearly depends on both the macro- and micro-mechanical response of the material. Essentially any local, microscale reduction in material strength or viscosity, whether preexisting or deformation-induced, is a potential shear band nucleation site. Moreover, the nucleation mechanism itself need not be thermally activated in order to give rise to an adiabatic shear band. Indeed, once shear flow localization starts, a significant contribution from thermal softening is inevitable provided only that deformation continue at a sufficiently high rate. Some postulated nucleation mechanisms include: grain boundary sliding, softening due to microvoid formation around inclusions or second-phase particles, polycrystal textural softening, anisotropic intragranular plastic response, release of dislocation pile-ups at grain boundaries, phase changes. It is clear that any complete model for distributed shear band damage must incorporate some description of material inhomogeneity at the microscale. It is worth noting that the model of Curran *et al.* [15, 16, 17] does so although in an indirect manner.

The requirements of large scale terminal effects simulation demand that shear band modeling be accomplished within a continuum formulation. This formulation should incorportate the effects of relevant micromechanics, yet be applicable at the length scale of computational discretizations[8] used in production armor/antiarmor simulations. Section 3.1 will describe a recent effort at BRL towards this goal. An alternative approach is that of Curran *et al. ibid*, described in section 3.2. In this approach a "microstatistical" description of shear band nucleation and growth is embedded within a continuum elastic-plastic formulation. Ultimately, models capable of handling both isolated and distributed shear bands are needed. For example, a large isolated band (e.g. a plug boundary) might be treated as a singular zone or surface (i.e. a slide line) which would possess a constitutive structure distinct from that of the surrounding material and determined by single-band modeling as discussed below. Distributed shear band damage should be amenable to statistical mechanical methods similar to those being developed to treat distributed crack damage in brittle materials by Dienes [81, 82]. The goal of such analysis is to obtain continuum formulations which incorporate the relevant micromechanics through an internal state variable structure. As with brittle cracks, the essential prerequisite for a statistical treatment is an adequate understanding of single- and few-band nucleation, growth and interaction problems.

Returning to modeling of shear band growth, we outline some efforts at BRL and elsewhere. Much work to date has focused on a one-dimensional "model problem" in which a slab of finite thickness and infinite in-plane extent is subjected to simple shearing, perhaps superimposed on uniaxial compression. This is the simplest geometrical context in which adiabatic shear localization can be studied,

[8]Typical mesh spacings are 0.01 to 1.0 mm, although for three dimensional simulations larger spacings are usually required.

but accurately simulates several important aspects of the "pressure-shear" tests of Clifton [83] and, somewhat less accurately, the thin-wall tube torsion test (see Hartley *et al.* [84]; Lindholm *et al.* [85]). If the velocity at the slab boundaries is held constant, the boundaries are thermally insulated and homogeneous initial conditions are imposed, then the system of field equations has a spatially *homogeneous* solution in which the mechanical fields are all functions of time alone. Since for metals the rate of strain hardening typically decreases with increasing temperature and strain, homogeneous deformation will initially yield monotone increasing shear stress followed by monotone decreasing shear stress after thermal softening dominates strain hardening. The basic picture of shear band formation which has emerged from analysis of the model problem and from related experiments is as follows: slow initial variation of fields (stress, temperature, strain rate, etc.) associated with perturbations or inhomogeneities, followed by relatively sudden localization (shear band formation), and then slower post-localization variation. If the region containing the shear band is also subjected to sufficient pressure, material failure may be considerably delayed or suppressed altogether.

4.1 Modeling of Individual Shear Bands

4.1.1 Onset of Localization

Loss of stability of the homogeneous solution (usually interpreted as infinitesimal stability) is a necessary (although *not* sufficient) condition for localization in the model problem. Early analyses (see Rogers [14]) focused on identification of the point on the homogeneous stress strain (s-γ) curve at which $ds/d\gamma$ vanishes, typically by using the flow law to expand $0 = ds$ and then estimating (or ignoring) various terms on the right hand side. Rigorous analyses of Wright and Walter [86, 87] and Wright [88] show that $0 = ds$ is generally *not* a sufficient condition for growth of perturbations, much less for shear band formation. Moreover, even after perturbation growth begins (e.g. the strain field begins to develop macroscopic inhomogeneity), shear band formation may not occur until much later. This delay in band formation has been observed experimentally by Marchand and Duffy [89]. Stability analysis of the model problem is complicated by the fact that the homogeneous solution is time-varying and so the linearized perturbation equations have time-varying coefficients. Many analyses ignore this and draw questionable conclusions based on constant-coefficient techniques. To date, no rigorous stability analysis exists for the model problem which includes all the important macroscopic material behavior: local conversion of plastic work to heat, local heat conduction, thermal softening, strain and strain rate hardening, inertia. Moreover, because shear band formation is a highly nonlinear process, linear analyses tend to provide primarily qualitative results. However, in several special cases important *scaling laws* have been obtained (e.g. Wright [88]) which

relate various material and problem dependent constants to critical onset parameters such as: imperfection sensitivity, shear band susceptibility, critical strain or temperature at shear band formation.

Two and three-dimensional extensions of this sort of analysis have also been published by Anand *et al.* [90, 91] in which (typically) a planar "shear band"-like velocity perturbation is superposed on a homogeneous shearing. The orientation of the shear band is given by a normal vector n whose value is obtained as part of a linear perturbation analysis. Critical conditions involving the state of homogeneous deformation, material parameters and band orientation are sought under which the perturbation fields grow rather than decay. More complete analyses are needed, especially those which: include nonlinear aspects of the problem (see Wright [92, 93]); pertain to previously unmapped regions of the parameter space (most analysis to date is based on a *quasi-static* approximation of the field equations); account for underlying deformations arising from nonproportional loading and anisotropic (e.g. single crystal) response.

4.1.2 Localization and Post-localization

The main objective in the model problem during and following rapid localization is to relate quantities describing the rapidity and severity of localization (peak strain rates and temperatures, rate of stress collapse, measure(s) of band width, etc.) to material and other pre-localization parameters. However, during rapid localization the governing equations are dominated by extremely nonlinear terms and no substantive analytical results exist. It is probable that some methods of combustion theory (e.g. activation energy asymptotics) may yield significant insight but application of these techniques is still in its infancy. Following localization at nominal strain rates appropriate to ballistic impact, complex wave phenomena occur (primarily due to the rapid drop in stress at the band core) which depend on the inertial, elastic, and thermoviscoplastic response of the material. Indeed, one of the most pressing needs for improved modeling is flow law data at temperatures from ambient to melting, strain rates up to $10^7 s^{-1}$ and strains up to 10 or more, see Walter [94]. Even numerical simulation can be difficult, and most numerical treatments to date have been exploratory or have involved limited parameter studies on various material parameters and the loading rate. The results of Batra and co-workers [95, 96, 97, 98, 99] may be the most extensive. It is clear that accurate, reliable simulation of single-band and few-band problems will require advanced adaptive numerical methods as are now being developed [100].

Some numerical results have been reported concerning band propagation in two dimensions; almost nothing has been reported in 3D. Most efforts have emphasized nucleation in that the band initiates from a defect, inhomogeneity or corner singularity and grows until stopping or reflecting at the domain boundary. Such studies are most relevant to distributed nucleation when they attempt to

model putative conditions at band nucleation (e.g. single crystal plasticity, stress contration at a grain boundary triple point, etc.) It is also essential that accurate numerical techniques be employed; many extant studies can be criticized because of artificial dependence on the computational mesh. Another difficulty is that, even with sufficient mesh refinement, the band structure may reach the domain boundary (ending the computation) well before it is fully developed. Edgewise band propagation speeds so obtained may bear little relation to those observed experimentally for well-formed band structures such as plug boundaries [101]. An effort is now underway at the BRL to simulate edgewise propagation of plug boundaries.

4.2 Modeling Large Scale Terminal Effects due to Shear Bands

The previous section has reviewed instances in which deformation localization in a viscoplastic medium into an individual shear band has been successfully modeled numerically. The necessary ingredients were seen to be the equations of motion, a flow law that includes explicit thermal softening, and a spatial discretization fine enough to resolve the deformation gradients. As seen in Figure 8, shear bands in RHA exhibit widths as small as 6 μm, and finite element edges in these analyses have been at least an order of magnitude smaller than this dimension. Since the total domain size has been limited to about 1 mm^2, it was feasible to employ such small elements.

When numerically simulating a macroscopic problem in terminal ballistics, such as target plate penetration by a long-rod penetrator or a shaped-charge jet, monetary cost and computer storage considerations prohibit the use of extremely small elements. The goal of explicit modeling of individual shear bands must be replaced by that of adequately introducing into the simulation the overall *effects* of shear banding. This generally involves supplementing the equations of motion and flow law with other ingredients needed to model distributed shear band damage. This section will review two instances of progress in this direction.

First is the modeling by Raftenberg at BRL of 12.7 mm-thick RHA plate perforation by a copper shaped-charge jet produced by a warhead fired at 15.3 C.D. standoff [102]. This work involved the insertion into Lagrangian hydrocode EPIC-2 [103] of an algorithm to model shear band effects. The algorithm consists of three parts: (i) a shear band onset criterion, (ii) a post-onset procedure for stress reduction, and (iii) the slideline erosion procedure that is included in EPIC-2 [104], and that is activated by a critical equivalent plastic strain, $\epsilon^p_{\text{erode}}$. All three parts are applied at the element level.

The onset criterion is based on a condition first proposed by Zener and Hollomon in 1944 [13], which states that shear banding results from the local excess

of the rate of thermal softening over the rate of work hardening. The strength model in EPIC-2 is the Johnson-Cook flow law [41], which expresses the flow stress in terms of separable factors involving work hardening, thermal softening, and strain rate hardening or softening as given by (5). At a given time step, in each element that has not yet satisfied the onset criterion, that is currently undergoing plastic flow, and that also underwent plastic flow at the preceding time step, the product of the first and last factors is compared with its value at the preceding time step (the factor involving $\dot{\epsilon}^p$ is not considered). If this product has diminished since the previous time step, the element is deemed to have undergone shear band initiation. The element's equivalent plastic strain at this time step is denoted $\epsilon^p_{\text{onset}}$.

The stress reduction algorithm used in Raftenberg's shear band modeling procedure is discussed next. Deviatoric stresses in an element that has satisfied the shear band onset criterion are, at all time steps thereafter, reduced from their values as computed without considering element damage. The hydrostatic stress is unaltered. The imposed deviatoric stress reduction is in proportion to the amount by which the element's equivalent plastic strain exceeds $\epsilon^p_{\text{onset}}$, so that

$$s_{ij} = s^*_{ij}\left(\frac{\epsilon^p - \epsilon^p_{\text{onset}}}{\Delta\epsilon^p_{\text{fail}}}\right), \tag{8}$$

where s_{ij} is the deviatoric stress tensor and s^*_{ij} is its value prior to reduction due to damage. The additional equivalent plastic strain beyond $\epsilon^p_{\text{onset}}$ corresponding to which the element's deviatoric stress is set to zero, $\Delta\epsilon^p_{\text{fail}}$, is introduced as an input parameter to characterize the material. It is observed that elements that have satisfied the onset criterion and that are then subjected to this stress reduction scheme become susceptible to large deformation.

Slideline erosion is used to model removal of fragmented target and projectile material. Since this removal is activated by a cutoff on equivalent plastic strain in an element on the slideline, elements that have satisfied the shear band onset condition and that thereafter experience large deformation become likely candidates for future erosion. In this way the connection between shear banding and fragmentation that was noted in Section 1.3 in the context of Figures 5 and 6 is introduced.

In [102] variation of the input parameters, $\Delta\epsilon^p_{\text{fail}}$ and ϵ_{erode}, and a negative pressure cutoff, p_{min} (used to model ductile void formation) affords good agreement with experiment in terms of final hole geometry and the time history of hole formation. It remains to be seen whether the parameter values that produce agreement with data for this particular case of standoff and target plate thickness will also produce agreement in other situations.

Workers at SRI International have developed a "microstatistical" approach to the problem of representing shear band effects in a macroscopic numerical analysis

[105, 106]. Their model has the ambitious goal of explicity tracking, by means of internal state variables, shear band properties, including their local density, size, and orientations. The material's macroscopic behavior is then related explicitly to these properties. The SRI model has six components:

1. a "nucleation threshold criterion", which specifies the conditions under which bands nucleate;
2. an assumed size distribution of shear bands at the time of nucleation;
3. an equation describing the rate of band nucleation;
4. an equation describing the growth rate of shear bands,
5. a model for the coalescence of shear bands to form fragment boundaries;
6. the effect on the stress tensor of the shear band distribution.

A number of micromechanical assumptions are introduced in the course of the development, and the model contains numerous parameters that characterize a material. These parameters have been evaluated for various steels and for DU at SRI by means of a "confined fragmenting cylinder" experiment.

The SRI model has been implemented into their working Lagrangian hydrocode, C-HEMP [107], and has been applied to at least two problems of interest to terminal ballisticians. One such problem involves a fragmenting munition [105]. The second problem involves perforation of an RHA plate by a rod composed of 4340 steel, where the geometry and impact velocity of the rod were varied [17]. Impact velocities considered were in the range of 500 to 1500 m/s. At the lower velocities predicted shear band damage was confined to a thin, cylindrical region propagating ahead of the penetration interface, consistent with the plugging mode of perforation observed in their accompanying experiments. At higher velocities the plugging mode gave way to more widely distributed damage, again in agreement with experiment.

More recently, the SRI model has been implemented into the widely-used Lagrangian hydrocode DYNA2D [108, 109]. This code includes an eroding slideline algorithm, so that the SRI model can now be applied to penetration problems for a longer duration than was possible with C-HEMP. The manner in which the SRI workers have integrated or replaced parts 5 and 6 of their procedure with the eroding slideline algorithm in DYNA2D has not yet been reported. A comparison with experiment of predicted hole geometry and shear band locations obtained with the SRI version of DYNA2D has also not been reported. The SRI approach, with its grounding in the microstatistics of shear bands, offers the promise of a quantitative understanding of the role of shear bands in determining macroscopic behavior. The need now is a validation of the approach by the application of

this version of DYNA2D to a wide range of ballistics problems. These should include penetrations by both shaped-charge jets and long rods into a wide range of materials.

4.3 Conclusions

Modeling the nucleation and growth of individual shear bands using continuum thermo-visco-plasticity theory has produced important insights into the fundamentals of this phenomenon. In 1-D, continued analytical work is needed to understand the kinetics of rapid localization. Simulations can be used to inexpensively explore the post-localization regime, perform parameter studies, and infer some of the consequences of improved plastic flow laws.

The very complex problem of distributed shear band nucleation must be addressed in at least a 2-D context; ultimately, a 3-D treatment will likely be required. Considerable care needs to be taken to model, to the extent possible, the actual material microstructures believed to contribute to nucleation. It is also to be expected that some of the more subtle aspects of thermo-visco-plasticity models (e.g. textural softening) will play a crucial role in quantitative simulation of nucleation. Analytical techniques which prove useful in quantifying the rapid localization régime in 1-D may be applicable in 2-D and 3-D as well. Multiple band interaction studies are barely into their infancy as yet. Nonetheless, a through understanding of the kinetics of band interaction is essential in order to construct a genuine statistical mechanics of distributed shear band damage and to obtain fully satisfactory continuum models for distributed damage and fragmentation.

The ability to simulate the effects of abiabatic shear bands in macroscopic terminal ballistics problems is a goal of great practical importance. Two reported approches have been discussed. The sanctioning of either as a predictive tool awaits further validation with experiment and the evaluation of input parameters for a variety of relevant materials.

5 Brittle Failure and Granular Flow of Ceramics (M. Scheidler, S. Segletes)

Unlike ductile metals, ceramics can undergo extensive microcracking when subjected to dynamic compressive loads. This compressive fracture degrades the elastic moduli, yield strength and tensile strength of the ceramic, resulting in more extensive fragmentation on the arrival of tensile reflections from free boundaries and material interfaces, and in the granular flow and subsequent bulking of comminuted material under shearing loads. The phenomenological observations in Section 1.2 and in Shockey *et al* [1?0] highlight the influence of these failure mechanisms on the penetration process. These phenomena account, at least in

part, for the lack of success in simulating the penetration of ceramic armor using traditional brittle failure models for metals.

Currently, within the DOD community (including DOD, DOE, contractors and universities) there is substantial experimental and modeling activity in the area of dynamic behavior of ceramics. The Ceramic Modeling Working Group (CMWG), hosted by Ed Cort of ATAC, Los Alamos National Laboratory, meets periodically and provides a forum for modelers to discuss ongoing issues of ceramic modeling. To date, more effort has been placed on the pre-failure behavior and the fracturing process than on the the post-failure response of ceramics.

In the sequel, the processes of dynamic fracture and the response of damaged but intact material are discussed first. This is followed by a discussion of the granular flow of a comminuted ceramic.

5.1 Dynamic Failure of Ceramics

Theoretical and experimental studies have identified a variety of possible mechanisms for compression-induced microcracking; e.g. crack initiation at grain boundaries, deformation twinning, axial splitting, shear faulting, and void collapse. The dominant mechanism may vary with purity, grain size and other microstructural features, as well as with temperature, strain rate and confining pressure; cf. [111, 112, 113, 114, 115, 116, 117, 118]. For both compressive and tensile failure, as strain rate increases the inertial dependence of crack instability and propagation results in a higher fracture strength and a wider range of cracks sizes activated nearly simultaneously. Thus damage tends to be more evenly distributed and fragment sizes tend to decrease with increasing strain rate; cf. [116, 118, 119, 120, 121, 122]. The extent of microcrack growth depends strongly on the duration of the stress pulse [115], and there is some evidence that crack instability is also dependent on pulse duration [123]. Other aspects of dynamic fracture are not well understood; e.g. the interaction of growing microcracks by means of stress waves, and the influence of inertial resistance to crack opening on the effective stiffness of microcracked bodies [121]. Even in the static case, crack interaction is an extremely complex problem. For example, recent work by Kachanov *et al.* [124] indicates that the effect of a distribution of microcracks on a macrocrack may range from shielding to amplification and cannot be modeled by replacing the microcracked material with an "effective" elastic material of reduced stiffness, as is often reported in the damage mechanics literature.

Much of the relevant data on dynamic behavior of ceramics comes from normal plate impact experiments. In some ceramics, compression-induced microcracking is observed below the Hugoniot elastic limit (HEL), while in others it does not occur until well above the HEL [115, 125]. The measured HEL's of many ceramics are substantially higher than the values calculated from quasi-static uniaxial strain tests (even after the correction for uniaxial strain) [9, 126]. HEL's of 2–3 times the

quasi-static values have been reported for alumina, with the differences attributed to strain rate dependence of yield strength by some authors and to pressure dependence of yield by others [126]. Plate impact experiments [9, 10, 127] indicate that beyond the HEL the shear strength of boron carbide decreases, the shear strength of alumina and aluminum nitride remains essentially constant, and the shear strength of silicon carbide and titanium diboride increases with increasing shear strain. Because of the high confining pressures, retention of shear strength and even increases in shear strength may be concurrent with extensive microcracking, as indicated by the loss of spall strength in AD-85 alumina, aluminum nitride and titanium diboride after sufficiently high shock loading [10, 127].

Constitutive models in production codes typically consist of equation of state models, elastic-plastic models for the deviatoric stress, simple failure criteria, and crude methods for post-failure strength reduction; cf. the discussion in Section 2. Even the more sophisticated models, such as the Hancock-MacKenzie (P/Y) model in HULL and the Johnson-Cook model in EPIC and DYNA, do not realistically treat the post-failure strength reduction. In particular, strength reduction is typically treated as isotropic. An exception is the oriented crack model (Material Type 17) in DYNA [27]; when a principal tensile stress excedes a critical value, the tensile and shear stresses are reduced on the plane normal to this principal direction. However, the rate of stress reduction has no physical basis; the model simply "reduces the stresses to zero over a small number of time steps". None of these models account for failure under overall compressive loads. Of course, it is possible to simulate a restricted class of experiments with a phenomenological model which does not directly account for compressive fracture. For example, uniaxial strain plate impact experiments have been simulated using a tensile failure model (for spall), together with a plasticity model which includes the dependence of yield strength and elastic moduli on such quantities as temperature, pressure, strain rate, and a scalar damage parameter (which evolves as a function of plastic work); cf. Steinberg [128] and Furlong *et al.* [129].[9] However, there is no evidence that such models can also be successfully applied to the dynamic behavior of ceramics under complex triaxial strain histories.

Of some relevance to ceramics are the Mohr-Coulomb type models which have traditionally been applied to geological materials and concrete; Material Models 16 and 25 in DYNA [27] and the Johnson-Holmquist model in EPIC [41] are of this type. These phenomenological models account (in a crude way) for failure under overall compressive as well as tensile stress states; the Johnson-Holmquist model also includes rate dependence of the failure surface. To account for the strength of fractured material under pressure, the DYNA Model 16 and the Johnson-Holmquist model incorporate a second pressure dependent yield surface

[9] Steinberg's simulations indicate that pressure dependence of the elastic shear modulus needs to be included to accurately predict the arrival time of release waves.

for failed material. However, shear-induced dilatancy, due initially to the opening of microcracks and later to the granular flow of comminuted ceramic, is not accounted for in a physically realistic way in any of these models; cf. the discussion in the next section.

None of the constitutive models currently incorporated in production codes have all the features necessary to predict the response of ceramic targets under the complex loading histories encountered in a ballistic impact. On the other hand, the problem of determining which features need to be included in a ceramic failure model has yet to be sorted out. Various brittle material modeling efforts have been put forward at the 7th CMWG meeting (Segletes, [130]) by Shockey (SRI), Rajendran (UDRI), Glenn (LLNL), Reaugh (LLNL), and Addessio (LANL). Failure models based on the nucleation, growth and coalescence of cracks would appear to have a good chance of predicting the time-dependent process of stress wave induced fracture. One of the earliest examples of this type (for tensile failure only) is the SRI BFRACT model [131]. Another example is the Statistical Crack Mechanics (SCM) model of Dienes [81, 82]. This model permits crack opening under tensile loads and crack growth under tension and shear. The growth of cracks in shear results in microcrack growth under compressive loads, so that the model directly accounts (at least in a crude way) for compression-induced failure. Strength degredation is based on an effective modulus theory, which naturally accounts for both rate and orientation dependence of the material strength. Crack coalescence is modeled by a strictly geometric process; mechanical interactions are neglected. The BRL is currently supporting further development of the SCM model and its implementation in the 3-D HULL code. Some of the features of the SCM model are incorporated in the brittle failure model of Addessio and Johnson [132].

One phenomenon which presents a difficult modeling problem is the formation of radial cracks under normal impact; cf. Section 1.2. Since this is initially an axisymmetric problem, the stress on every radial plane is the same prior to the formation of these cracks, so that all radial planes are equally likely to fail. The models discussed above would thus predict simultaneous failure on all radial planes. However, only a discrete number of radial cracks are observed. An energy-based fracture analysis (cf. [120, 122]) might prove useful here.

5.2 Granular Flow

The granular flow of brittle materials under impact is a topic which currently concerns experimenters and code developers alike in the ballistics community. When considering ballistic penetration into ceramics, it becomes clear that a significant percentage of the penetration process takes place into fractured ceramic. The diversity of behavior that surely must occur under these circumstances is daunting to the modeler: dilatancy effects, which cause the rubble to bulk in volume under

the effects of shearing; Coulomb frictional behavior which inhibits rubblized flow in a manner directly related to the confining pressure of the rubble; and of course the granular flow behavior itself, which we should have no reason to believe follows the simple coaxial flow laws of metallic plasticity. With this as the situation, it seems a foregone conclusion that the mechanics of dilatancy, friction and granular flow be incorporated into the brittle material models of today's hydrocodes. Unfortunately, the reality of the situation is not so simply addressed.

Experimentally, it was only early in 1991 that Grady of SNL [133] devised a uniaxial plate impact test to load, unload, then reload a ceramic specimen, in hopes of ascertaining the stress-strain behavior of comminuted ceramic.

The small number of hydrocodes currently possessing an operational ceramic model handle the difficult problem of granular flow in a simplistic ad hoc fashion. For example, the Johnson-Holmquist model [41] implemented in the EPIC code effects a one-time, instantaneous, pressure increase at the onset of "fracture" (i.e. when a scalar damage parameter equals unity), which is intended to account for the dilatancy of comminuted material as a result of granular flow. Scheidler reports [134] that this model is being modified to avoid the instantaneous stress transitions which characterized failure in the original model implementation. Note however, that this "dilatacy" effect in EPIC is not explicitly related to shearing strain or its rate, as the classical definition of dilatancy would lead us to believe, but is rather tied to the energy of compressive volumetric deformation. To further illustrate the simplistic nature of current ceramic model development, consider the presentation of Henninger (of LANL) to the 7th CMWG [130], in which he described his efforts to put the Johnson-Holmquist model into the Eulerian MESA code. The question arose as to how the model's scalar damage parameter, which triggers "instant" failure, could be a properly advected quantity. Without special ad hoc provisions made by Henninger and his colleagues, the implementation would have permitted failed ceramic material to "unfail", simply by diffusing its damage over several cells, thus bringing the damage level below the threshold value for "failure".

Segletes [135] has also presented hydrocode modeling efforts that deal with the "bulking" (i.e. dilatancy) of ceramic rubble upon failure. Yet here again, the evolution of his bulking terms are not tied to shearing rate. The ability of this model to adequately address granular flow must thus be called into question. Other recent efforts to model the ballistic behavior of ceramics with hydrocodes ignore the mechanics of granular flow altogether. An exception is the modeling reported at the 7th CMWG meeting by Shockey (the model is actually that of Curran, Seaman and Cooper [136]).

The granular flow problem is, by no means, an easy one to resolve. One obvious difficulty is the need to model the essentially discontinuous process of granular flow in the continuum framework of the hydrocode. Additionally, existing treatments of low pressure granular flow (e.g. in the soil mechanics literature),

which might otherwise provide guidance for the the ceramic model developers, tend to be characterized by a large and "rapidly increasing" number of material parameters "which defy physical intuition" (Scott, [137]). On the experimental side, it is difficult to create controlled granular flow conditions under the pressures and strain rates characteristic of ballistic impact.

Micro-mechanical modeling of high pressure granular flow is being done by Nemat-Nasser and Balendran [138] at the University of California San Diego (UCSD), by Jenkins [139] at Cornell University, and by Curran, Seaman and Cooper [136] of SRI. The UCSD model is based on the frictional effects of sliding granules, while the Cornell model, because of its analogy to the kinetic theory of gases, focuses on the collisional behavior of a granular mass. What separates these models from others being developed for and implemented in hydrocodes is the fact that the actual micromechanics of interacting granules are considered in the derivation of the models, while at the same time the final form of the governing equations are continuum relations amenable to hydrocode implementation. It still remains to be seen how easily the material parameters characterizing these models can be measured.

5.3 Conclusions

Models for ceramic materials and their implementation into hydrocodes is currently in a great state of flux, as noted by Segletes [130] in his trip report from the 7th Ceramic Modeling Working Group meeting:

> A variety of ceramic models are being proposed and some of them are being implemented into hydrocodes. What [is striking] was how each computational result presented seemed different in fundamental ways: some caused damage only under the penetrator while others created damage only upon tensile reflection at locations distant from the penetrator; some created a relatively small zone of damage, while others created vast zones of debris; some models propagated damage slowly with others advanced it rapidly; some ceramic bulked while other did not; some rubble was frictional while other was not; etc.

As more experiments with detailed records become available, the mettle of these new ceramic models can be put to the test. It is too early, at this time, to tell how useful the simpler treatments of ceramic modeling in today's hydrocodes will be, but it is anticipated that modeling which specifically addresses the mechanics of compressive fracture and flowing granules might be necessary to provide the predictive capability sought by today's armor designers.

6 Equation of State (S. Segletes)

The equation of state (EOS) provides an analytical tool by which the pressure-volume-energy state of a material may be predicted as the result of a thermodynamic transition of the material. In contrast to tabulated or graphical state data, where hundreds or thousands of data points may be obtained to characterize the state of a material over a range of states, the equation of state, comprised of semi-empirical functional forms to which experimental data are fit, may require only a few independent parameters to characterize. Correspondingly, relatively few data points are typically acquired to characterize the EOS parameters. Often, these data are clustered along a particular thermodynamic path (e.g. the Hugoniot, for high pressure behavior), while the behavior off of this path is linearized (e.g. as in the case of the Mie-Grueneisen EOS).

In small strain models, an equation of state is generally not employed. Rather, the hydrostatic component of stress is simply computed as the product of the bulk modulus and the volumetric strain. When the pressure-volume relationship is known to be non-linear, or when energy becomes coupled with the pressure, as in the case of impact events, an equation of state must be used. In hydrocodes, where event durations to be modeled are typically in the microsecond timeframe, adiabaticity is a valid and almost universal assumption. However, for cases intermediate to small strain and violent impact, neither constant compressibility nor adiabatic assumptions are warrented, and heat transfer can become a significant term, which will affect the pressure calculation. Such intermediate cases are not well handled by today's hydrocodes, which generally ignore the effects of heat transfer altogether. A heat conduction option was, in fact, employed in versions of EPIC2 through the 1980's, but seems to have been dropped when the EPIC2 and EPIC3 codes were combined into a single (1D, 2D, 3D) EPIC code [28].

Problems may arise in the application of equations of state in hydrocodes, not only because of the sparse data which was used to characterize them, but for a variety of other reasons. Segletes [140] points out a variety of problems which arise in the development and application of many of today's hydrocode EOS models. They include:

1. Permitting the use of an EOS model in a manner which violates the limitations and/or assumptions of the model. Examples of this problem include EPIC [28] and HULL [24, 141, 142, 143], which do not limit the compression range over which an EOS model may be used to those compressions where the data fit is valid.

2. Relying on heuristic material models to the extent where the models become institutionalized and taken as fact by an unknowing user community. Examples of this are the porous material models found in several hydrocodes.

The HULL code manual does a good job of describing the ad hoc nature of its geological model, going to the extent of warning the user about using this Hugoniot model in various stress regimes. The EPIC manual [28] refers to a version of the HULL model for EPIC's "crushable solid" model, but simply describes the mathematics of the model, and not its heuristic foundations. The CTH code [144] uses a porous material model, and even assigns it the appellation "Snowplow model". No reference or technical description is given, though a warning about not using it for partially crushed states is provided.

3. Making ad hoc modifications to older, well founded EOS models, rather than rederivation from basic principles. For example, the EPIC code uses the same set of pressure-energy equations to handle expansion as well as compression, and thus makes the (presumably) unintended assumption of a tensile shock.

4. Dissemination of undocumented material libraries. HULL and, to a lesser extent, MESA are offenders in this regard. Such actions promote the uninformed use of data of unknown origin.

In addition to these problems, EOS models which reference all thermodynamic states back to a Hugoniot reference curve (e.g. the Mie-Grueneisen EOS), can suffer from problems which depend on the impact velocity regime of application. For low impact velocities, use of the shock Hugoniot reference curve is not correct, since conditions will tend to be isothermal, rather than adiabatic. As contact velocity increases, plastic work will increase, tending to move the thermodynamic state further from the Hugoniot reference curve. Since the Mie-Grueneisen EOS is linearized about this reference, the accuracy in modeling these non-Hugoniot states is reduced. In the hypervelocity impact régime, additional issues need to be considered. Material phase changes may play a significant role in the event but are not addressed by the Mie-Grueneisen EOS. Finally, Segletes [140] has shown that improper formulation of the Grueneisen parameter can, in cases of hypervelocity impact, overdrive the EOS into inaccurate or even unstable regimes. All codes in his study (i.e. EPIC, HULL, DYNA, MESA, and CALE) were shown to be susceptible to this mode of instability.

The talk here has concentrated on the Mie-Grueneisen EOS, because of its pervasive use in the hydrocode community. Other options in equation of state modeling are however, available. Probably the second most popular form in hydrocodes is the Tillotson equation of state [145] which is generally applicable at much higher pressures than is Mie-Grueneisen. Tillotson provides a form which essentially allows the Grueneisen coefficient to be a function of internal energy, as well as volume. In this manner, behavior at lower pressures can be smoothly transitioned to Thomas-Fermi-Dirac statistical theories at higher pressures.

The fundamental understanding of equations of state are very good, in general. However, as applied in today's hydrocodes, several admonitions are applicable:

1. Ad hoc material models serve a need, but are no substitute for a properly founded model.

2. Characterizing a complicated material behavior in terms of a small handful of material parameters can lead to thermodynamic inaccuracies and even instabilities in various locations in thermodynamic space.

3. As with all models, users must understand and adhere to limitations and assumptions of EOS models as well as material data. These limitations and assumptions are not always known to the code user community, since they are often ignored or glossed over in code documentation.

4. Code developers have the responsibility to document material properties, if provided with the code.

5. Correspondingly, code users have the responsibility to understand and know the origin of the material inputs used in the code.

7 Summary of Important Points and Pressing Needs (T. Wright)

For the most part, the comments in this section are amplified and illustrated at the appropriate place in the body of the report, although the emphasis in some cases may reflect only the particular views and biases of the present writer. In any case, the intent of this section is to highlight particularly important points of the main discussion. These are noted in the boldface paragraphs below. Each point is followed by a few words of justification and then by a short bulleted list of tasks that should go far toward advancing the state-of-the-art in one particular area.

"Substantial progress will proceed from accurate simulation of carefully controlled experiments."

This statement, taken from the summary of Section 2.2, was intended to apply to the mechanics of penetration of ceramic targets, but it applies equally well to penetration of metallic targets and to material characterization tests of both ceramics and metals. Thus it may be taken as a kind of credo underlying this whole report. There is a hidden requirement, however. Namely, before it is possible to

achieve accurate numerical simulation of a complex experiment, it is first necessary to model the material response accurately. It is usually assumed that the pointwise response of a material is the same as its response to homogeneous deformation. Consequently the simplest characterization experiments are designed to achieve essentially homogeneous deformation over a gauge section that is large enough to provide access for measurements. When this is achieved, there is no real need for simulation. However, because of wave propagation, rate effects, complex test sequences, and the difficulty of enforcing (pointwise) boundary conditions for complex specimen geometries, it is often not possible to achieve the degree of homogeneity necessary for direct interpretation of measurements. This is especially true for experiments involving finite and/or high-rate deformations; homogeneity is definitely not available as a simplifying construct in ballistic testing. Under these circumstances simulation is essential for all but the crudest interpretation of experiment.

- There is a need for accurate material models for use in numerical simulation of ballistic events. In many cases numerical simulation is also needed to help interpret high rate material tests.

Material modeling in ballistics must start with observed phenomenology.

This statement may seem obvious, but it cannot be overemphasized. The violent physical environment of penetrator formation and ballistic impact is far from the usual training and experience of most engineers and scientists. In fact the pressures, strains, and strain rates routinely encountered in ballistics (averages of the order of 10 GPa, 1.0, and $10^4 s^{-1}$ to $10^5 s^{-1}$, respectively, with much higher peaks, [1]) are difficult to reproduce in controlled laboratory experiments for material characterization. By answering key phenomenological questions such as "Where does the material go?", "Where, when, and how does it deform and fail?", or "What forces exist in the material to make these things happen?" the experimental ballistician can provide the facts that challenge those who develop material models.

- There is an overwhelming need for careful, diagnostic experiments on ballistic phenomenology. Time resolved experiments at fixed locations and time sequences of spatially resolved observations are generally more useful than simple post mortem measurements. Microscopy can be used to determine the material mechanisms of deformation and failure.

There are significant differences in the response of metal and ceramic targets.

Again this statement may seem obvious, but the differences are often underestimated in planning and interpreting ballistic experiments. Because metals can experience large plastic deformations, they are not greatly altered by the passage of the initial shock wave, and a sort of quasi-steady process zone can form at the penetrator/target interface. This is particularly evident for long rod penetrators.[10] On the other hand, ceramics experience little or no plastic deformation before degradation sets in so they are very sensitive to the intensity of wave fronts and wave interactions. If process zones do form in ceramics, they may be vastly different from those that form in metals.

- There is a need for simple, but realistic, models of penetration into ceramics.

The principal numerical methodologies in use today for large scale numerical simulations of ballistic impacts each have characteristic drawbacks.

Since Eulerian schemes average the field quantities over a computational cell, boundaries between different materials tend to become blurred through a kind of numerical diffusion that is wholly artificial. Lagrangian schemes can preserve material boundaries by suitably locating the grid points, but easily fail through grid tangling or excessive distortion, usually near stagnation points. Other kinds of material discontinuities, such as wave fronts, elastic/plastic boundaries, or failure boundaries, tend to become indistinct in either scheme because they will not generally lie along predetermined grid lines. Eroding interface algorithms in Lagrangian codes achieve significantly longer run times, but at the cost of modeling the dominant physical process with a numerical artifice. Arbitrary Lagrangean Eulerian (ALE) type codes, now coming onstream, would seem to have great potential for capturing the best features of both major types while avoiding their worst drawbacks, but experience with these codes is still limited.

- There is a need for better algorithms to track material boundaries in Eulerian codes, and to track other kinds of discontinuities in both Eulerian and Lagrangean codes.

- There is a need for algorithms to treat flow near a stagnation point in Lagrangean codes so as to achieve unlimited run times without sacrificing accurate physical modeling.

[10]The consequences of this process zone in the penetrator have been explored by Wright and Frank [146] , who noted that "target resistance" involves characteristics of the rod and of the specific collision under consideration, as well as the flow stress in the target. Thus the concept of intrinsic target resistance, although often useful, does not seem to hold strictly for metals any more than it does for ceramics.

- There is a need to learn how to control and optimize the grid motion in ALE-type codes.
- There is a need for adaptive gridding algorithms that dynamically move, refine, or coarsen the computational grid in response to the deformation so as to achieve the highest resolution in regions with high gradients in the field quantities.

All computing techniques in current terminal effects codes fail where highly localized deformation occurs.

Physical processes, such as the formation of tensile voids, adiabatic shear bands, or extensive microcracking, can produce strain softening and subsequently lead to severely localized deformations that are well beyond the resolution of any reasonable grid scheme. Examples are spall planes or plug boundaries, which should form in a calculation as a natural consequence of physical processes. Failure to resolve the deformation adequately in the neighborhood of the localization always leads to an overprediction of flow stress. In other words, the finite grid size itself becomes a (nonphysical) material property.

- There is a need to learn how to simulate the effect of localization without resort to ultrafine gridding.

Theories of finite plastic deformation are still under development.

Any continuum theory of material behavior must be based upon sound kinematics and must be properly invariant under rigid body rotations. In addition, there are special requirements for a theory in order that it be suitable for application to termianl ballistics. It must be accurate for finite elastic volume changes because of the large pressures that may be achieved under impact, but it only needs to account for small elastic distortions since deviatoric stresses are limited by the onset of plastic flow or fracture processes. It should also be accurate for large, monotonic plastic strain and for one reversal of loading or one large path change in stress space[11], but it need not be accurate for further cylic deformation. The assumption of plastic incompressibility seems to be adequate for most purposes. Although most (but not all) structural alloys are relatively insensitive to strain rate, the rates experienced in ballistic events are so large that it is better to include the effect. Thermal effects are important both in regions of large elastic volume change and in regions with large plastic working.

- There is a need for continued theoretical development of finite deformation plasticity that is tailored to the requirements of impact problems. Correct

[11]Typical loading and deformation histories, as experienced along a material flow line during penetration, have been calculated by Lin and Batra [147].

rate equations and the effect of large volume changes seem especially important. Although it is desirable that theories be motivated by micromechanical considerations, it is only necessary to achieve macroscopic fidelity.

- To achieve widespread acceptance there is a need to develop an extensive library of physical properties and elementary material response functions. For economic reasons then, the theory should be based only on standard physical properties, and should require only macroscopic characterization of materials as extensive microscopy is generally too time consuming and too expensive for routine use.

- There is a need for high rate testing roughly in the range of $10^2 s^{-1}$ to $10^5 s^{-1}$. Jump tests from one rate to another should be useful for discriminating between theories. Quasi-static tests are needed only to establish a baseline. Testing at all rates should extend to strains of order 1.0 or larger. This can often be obtained in a sequence of tests, if not in a single test.

- There is a need for testing in an extended temperature range, say from $-100°$ C to 2/3 the melting temperature with most testing taking place within a few hundred degrees of ambient. Tests at elevated temperatures should use the highest heating rates possible so as to suppress diffusive effects.

- It would be useful to devise high rate tests with nonproportional load paths. It would be particularly useful if those tests simulated a load path characteristic of ballistic impact.

Rate effects in the material response, whether in the plastic flow or in the fracture properties of the target or the penetrator, imply that there will be scale effects in ballistic testing.

Either a penetrator or a target will be more effective in small scale than in large scale if its material exhibits a strong strengthening rate effect. This is because local strain rates can be expected to scale as V_0/R, the striking velocity divided by the penetrator radius. Thus at the same impact speed, strain rates will be higher and loading times shorter in the smaller scale experiment. As a consequence the material will appear to be stronger in smaller scale.

- There is a need for ballistic testing at different physical scales when either of the materials involved has a strong rate effect in its material response. When both penetrator and target materials exhibit rate effects, the relative increase in dynamic strength is indeterminate.

Adiabatic shear banding is a major mechanism of damage and material erosion in ballistic events.

Plugging in metallic targets, which has been known for a long time, and newer evidence on penetrator erosion indicate the truth of this statement. Theoretical and experimental study of the phenomenon continues as a major research thrust today. It is now known from experimental studies [89], confirmed by computational work [96], and explained by theoretical work [88, 92] that a decrease in the flow stress does not necessarily indicate incipient localization although localization can be expected to occur somewhat later. Rate effects, heat conduction, and inertia all have the effect of delaying catastrophic loss of strength for some time after thermal softening has overpowered strain rate and work hardening in a ductile material.

- There is a continuing need to increase understanding of the fundamental kinetics of adiabatic shear banding.
- There is a need for developing multidimensional damage models that use kinetics as understood from more fundamental one dimensional studies.
- Although there is a need for more data on rate and temperature effects in plastic deformation, it is probably not necessary to obtain data at the extreme rates and temperatures that occur in the core of a fully developed shear band. This is because extreme conditions only occur after localization, not before. Furthermore, there is the prospect of describing the effect of the shear band on the surrounding material without resolving the full structure of the band itself, much as is now done with shock waves.
- There is a need to develop experimental techniques that, in a fundamental way, will allow comparison of the susceptibility to shear bands in different materials. Of course adiabatic shear bands can be formed in many materials by many different experimental techniques. The difficulty here is that shear band formation is an essentially inhomogeneous phenomenon that happens because of material instability. Without inhomogeneity no localization can occur, but in real materials and real loading situations there are always inhomogeneities of unknown or uncontrolled magnitudes. Consequently current measures of material susceptibility, such as ambient strain just prior to localization, have no value for comparing one material against another.

The inherently brittle nature of ceramics presents difficulties in material modeling for ballistic applications that are wholly different from those in ductile materials.

Ceramics exhibit initiation and extension of microcracking under compressive loads [112-119]. Since small fractures take time to accelerate, the failure process is effectively rate dependent. At slow loading rates, the weakest point cracks first

and then may dominate subsequent failure. At high loading rates, many points can reach critical levels before the weakest point gives way, so that many fracture sites may be activated. At very high loading rates and very high pressures, as in shock waves, massive fracturing and rubblization may occur, especially in reflected waves where mode conversion takes place. One major consequence of the rate dependence of compressive failure in ceramics is that ballistic tests are *not* scale independent.

- There is a need to develop high rate compressive damage and failure models for ceramics.
- In numerical simulation of either characterization tests or ballistic tests in ceramics there is a need to resolve elastic wave fronts and interactions because there is little plastic flow before failure.
- There is a need for material models for high speed flow of a granular material. The important points here are the process of conversion from intact material to fully comminuted material and the interaction of presure, volume, and shearing in a high speed flow. In some cases the volume expansion that accompanies comminution can be substantial.

Even though there is a large amount of accurate data and information available concerning equations of state, current codes do not always implement EOS models correctly.

- There is a need for better documentation and care in applications in numerical simulation, rather than a need for new EOS models.

References

[1] W. Herrmann. Materials response to ultra-high loading rates. Technical Report NMAB-356, National Academy of Sciences, Washington, D. C., 1980.

[2] Thomas W. Wright. A survey of penetration mechanics for long rods. In Jagdish Chandra and Joseph E. Flaherty, editors, *Computational Aspects of Penetration Mechanics*, volume 3 of *Lecture Notes in Engineering*, pages 85–106. Springer-Verlag, 1983.

[3] Garrett Birkhoff, D. P. MacDougall, E. M. Pugh, and G. I. Taylor. Explosives with lined cavities. *J. Appl. Phys.*, 19(6):563–582, 1948.

[4] A. Tate. A theory for the deceleration of long rods after impact. *J. Mech. Phys. Solids*, 15:387–399, 1967.

[5] A. Tate. Further results in the theory of long rod penetration. *J. Mech. Phys. Solids*, 17:141–150, 1969.

[6] V. P. Alekseevski. Penetration of a rod into a target at high velocity. In *Combustion, Explosion, and Shock Waves*, volume 2, pages 99–106. 1966.

[7] Konrad Frank and John Zook. Energy efficient penetration and perforation of targets in the hypervelocity regime. *Int. J. Impact Engng*, 5:277–284, 1897.

[8] B. L. Morris and C. E. Anderson. The ballistic performance of confined ceramic tiles. In *Proceedings of the 1991 TACOM Combat Vehicle Survivability Symposium*. U. S. Army Tank Automotive Commmand, 1991.

[9] Marlin E. Kipp and Dennis E. Grady. Shock compression and release in high-strength ceramics. Tech. Rep. SAN89-1461, Sandia National Laboratories, Albuquerque, NM, 1989.

[10] Dennis E. Grady. Dynamic material properties for armor ceramics. Tech. Rep. SAN91-0147, Sandia National Laboratories, Albuquerque, NM, 1991.

[11] Henri Tresca. On further applications of the flow of solids. *Proc. Instn Mech. Engrs*, 30:301–345, 1878.

[12] W. Johnson. Henri Tresca as the originator of adiabatic heat lines. *Int. J. Mech. Sci.*, 29:301–310, 1987.

[13] C. Zener and J. H. Holloman. Effect of strain rate upon plastic flow of steel. *J. Appl. Phys.*, 15:22–32, January 1944.

[14] Harry C. Rogers. Adiabatic plastic deformation. In R. A. Huggins *et al.*, editors, *Ann. Rev. Mater. Sci.*, volume 9, pages 283–312. Annual Reviews, Inc., 1979.

[15] Donald R. Curran *et al.* Computational model for armor penetration 1st annual report. Contr. Rep. BRL-CR-584, U. S. Army Ballistic Research Laboratory, Aberdeen Proving Ground, MD 21005-5066, October 1987.

[16] Donald R. Curran *et al.* Computational model for armor penetration 2nd annual report. Contr. Rep. BRL-CR-585, U. S. Army Ballistic Research Laboratory, Aberdeen Proving Ground, MD 21005-5066, October 1987.

[17] Donald R. Curran *et al.* Computational model for armor penetration 3rd annual report. Contr. Rep. BRL-CR-586, U. S. Army Ballistic Research Laboratory, Aberdeen Proving Ground, MD 21005-5066, October 1987.

[18] H. C. Rogers and C. V. Shastry. Material factors in adiabatic shear bands in steels. In Marc A. Meyers and Lawrence E. Murr, editors, *Shock Waves & High-Strain-Rate Phenomena in Metals*, pages 285–298. Plenum Press, 1981.

[19] J. H. Beatty, L. W. Meyer, M. A. Meyers, and S. Nemat-Nasser. Formation of controlled adiabatic shear bands in AISI 4340 high strength steel. Tech. Rep. MTL TR 91-4, U. S. Army Materials Technology Laboratory, Watertown, MA 02172-0001, 1990.

[20] K. Eckelmeyer. *The Diffusional Transformations, Strengthening Transformations, and Mechanical Behaviors of Uranium Alloys*, volume 1, pages 129–202. 1981.

[21] W. Gurwell, R. Nelson, G. Dudder, and N. Davis. Fabrication and properties of tungsten heavy metal alloys containing 30% to 90% tungsten. Tech. Rep. PNL-5218, Pacific Northwest Laboratory Report, September 1984.

[22] Lee S. Magness and T. Farrand. Deformation behavior and its relationship to the penetration performance of high-density KE penetrator materials. In *Proceedings of the 1990 Army Science Conference*, West Point, NY, May 1990.

[23] William Bruchey, Edward Horwath, and Priscilla Kingman. The effect of crystallographic orientation on the performance of single crystal tungsten sub-scale penetrators. In *Proceedings of the 1990 Army Science Conference*, Durham, N.C., May 1990.

[24] D. A. Matuska and J. J. Osborn. *HULL Technical Manual, Volume I.* Orlando Technology Incorporated, 1986.

[25] David A. Mandell *et al.* *MESA-3D Input Manual.* Los Alamos National Laboratory, March 1991.

[26] J. Michael McGlaun *et al.* CTH user's manual and input instructions, version 1.020. Tech. Rep. SAND88-0523, Sandia National Laboratories, 1988.

[27] Robert G. Whirley and John O. Hallquist. DYNA-3D—a nonlinear, explicit, three-dimensional finite element code for solid and structural mechanics—user manual. Technical Report UCRL-MA-107254, Lawrence Livermore National Laboratory, May 1991.

[28] Gordon R. Johnson and R. A. Stryk. User instructions for the 1990 version of the combined (1D, 2D, 3D) EPIC code. Final technical report under contract DE-AC04-87AL-42550, DARPA, 1990.

[29] J. N. Johnson and F. L. Addessio. TEPLA-F: Tensile plasticity and ductile fracture. *J. Appl. Phys.*, June 1988.

[30] B. I. Bennett *et al.* Recent developments in the SESAME equation-of-state library. Tech. Rep. LA-7130, Los Alamos Scientific Laboratory, 1978.

[31] Gerald I. Kerley. CTH reference manual: The equation of state package. Tech. Rep. SAND91-0344, Sandia National Laboratories, May 1991.

[32] S. L. Thompson. Improvements in the CHARTD radiation-hydrodynamics code III: Revised analytic equation of state. Tech. Rep. SC-RR-710714, Sandia National Laboratories, March 1972.

[33] M. van Thiel. Compendium of shock wave data, vols 1–3. Tech. Rep. UCRL-50108, Rev. 1, Lawrence Livermore Laboratory, 1977.

[34] S. P. Marsh. *LASL Shock Hugoniot Data.* University of California Press, Berkeley, CA, 1980.

[35] B. J. Kohn. Compilation of Hugoniot equations of state. Tech. Rep. AFWL-TR-69-38, Air Force Weapons Laboratory, 1969.

[36] D. J. Steinberg. Equation of state and strength properties of selected materials. Tech. Rep. UCRL-MA-106439, Lawrence Livermore National Laboratory, 1991.

[37] B. M. Dobratz and P. C. Crawford. LLNL explosives handbook. Tech. Rep. UCRL-52997, Lawrence Livermore Laboratory, 1985.

[38] M. L. Wilkins. Calculation of elastic-plastic flow. In B. Adler, S. Fernback, and M. Rotenberg, editors, *Methods of Computational Physics*, volume 3. Academic Press, 1964.

[39] M. L. Wilkins. Calculation of elastic-plastic flow. Technical Report UCRL-7322, Rev. 1, Lawrence Livermore Laboratory, 1969.

[40] Gordon R. Johnson and W. H. Cook. A constitutive model and data for metals subjected to large strains, high strain rates, and high temperatures. In *Proceedings of the Seventh International Symposium on Ballistics*, pages 541–548, The Hague, The Netherlands, April 1983.

[41] F. J. Zerilli and R. W. Armstrong. Dislocation-mechanics-based constitutive relations for material dynamics calculations. *J. Appl. Phys.*, 61:1816–1825, 1987.

[42] Gordon R. Johnson and T. J. Holmquist. Test data and computational strength and fracture model constants for 23 materials subjected to large strains, high strain rates, and high temperatures. Tech. Rep. LA-11463-MS, Los Alamos National Laboratory, January 1989.

[43] Lee S. Magness, 1991. Private communication.

[44] Paul S. Follansbee. Recent results and continued development of the MTS model. Tech. Rep. LA-UR-88-2521, Los Alamos National Laboratory, 1988.

[45] D. J. Steinberg, S. G. Cochran, and M. W. Guinan. A constitutive model for metals applicable at high-strain rate. *J. Appl. Phys.*, 51, 1980.

[46] D. J. Steinberg and C. A. Lund. A constitutive model for strain rates from 10^4 to 10^6 s^{-1}. *J. Appl. Phys.*, 65:1528–1533, 1989.

[47] Lynn Seaman. In W. Pilkey and B. Pilkey, editors, *Shock and Vibration Computer Programs: Reviews and Summaries.* Shock and Vibration Information Center, Washington, D. C., 1975.

[48] J. A. Zukas. Stress waves and fracture. In T. Z. Blazynski, editor, *Materials at High Strain Rates.* Elsevier, 1987.

[49] F. R. Tuler and B. M. Butcher. A criterion for the time dependence of dynamic fracture. *Int. J. Fract. Mech.*, 4, 1968.

[50] Lee Davison and Marlin E. Kipp. Theory of spall damage accumulation in ductile metals. *J. Mech. Phys. Solids*, 25, 1977.

[51] Gordon R. Johnson. Status of the EPIC codes, material characterization and new computing concepts at honeywell. In Jagdish Chandra and Joseph E. Flaherty, editors, *Computational Aspects of Penetration Mechanics*, volume 3 of *Lecture Notes in Engineering*, pages 24–35. Springer-Verlag, 1983.

[52] Lynn Seaman and D. A. Shockey. Models for ductile and brittle fracture for two dimensional propagation calculations. Technical Report AMMRC-CTR-75-2, Army Materials and Mechanics Research Center, 1975.

[53] Lynn Seaman *et al. J. Appl. Phys.*, 47:4814, 1976.

[54] D. C. Erlich *et al.* Further development of a computational shear band model. Tech. Rep. AMMRC-TR-80-3, Army Materials and Mechanics Research Center, 1980.

[55] Gordon R. Johnson and T. J. Holmquist. A computational constitutive model for brittle materials subjected to large strains, high strain rates and high pressures. In *EXPLOMET '90*, August 1990.

[56] R. Hill. *The Mathematical Theory of Plasticity.* Oxford, 1950.

[57] L. E. Malvern. *Introduction to the Mechanics of a Continuous Medium.* Prentice-Hall, 1969.

[58] W. Prager. A new method of analyzing stresses and strains in work-hardening plastic solids. *J. Appl. Mech.*, 23:494–496, 1956.

[59] H. Ziegler. A modification of Prager's hardening rule. *Q. Appl. Math.*, 17:55–65, 1959.

[60] L. W. Hu, J. Markowitz, and T. A. Bartush. A triaxial-stress experiment on the yield condition in plasticity. *Expl Mech.*, 6:58–64, 1966.

[61] P. G. Hodge, Jr. Discussion of [58]. *J. Appl. Mech.*, 24:482–483, 1957.

[62] G. Jaumann. *Grundlagen der Bewegungslehre.* Leipzig, 1905.

[63] John K. Dienes. On the analysis of rotation and stress rate in deforming bodies. *Acta Mech.*, 32:217–232, 1979.

[64] J. C. Nagtegaal and J. E. de Jong. Some aspects of non-isotropic workhardening in finite strain plasticity. In E. H. Lee and R. L. Mallett, editors, *Plasticity of Metals at Finite Strain: Theory, Computation and Experiment.* Stanford University, 1982.

[65] A. E. Green and P. M. Naghdi. A general theory of an elastic-plastic continuum. *Arch. Rational Mech. Anal.*, 18:251–281, 1965.

[66] R. J. Asaro and J. R. Rice. Strain localization in ductile single crystals. *J. Mech. Phys. Solids*, 25:309–338, 1977.

[67] Sia Nemat-Nasser. On finite deformation elasto-plasticity. *Int. J. Solids Struct.*, 18:857–872, 1982.

[68] E. H. Lee and R. L. Mallett. Stress analysis for anisotropic hardening in finite-deformation plasticity. *J. Appl. Mech.*, 50:554–560, 1983.

[69] Y. F. Dafalias. Corotational rates for kinematic hardening at large plastic deformations. *J. Appl. Mech.*, pages 561–565, 1983.

[70] G. C. Johnson and D. J. Bammann. A discussion of stress rates in finite deformation problems. *Int. J. Solids Struct.*, 20:725–737, 1984.

[71] Gordon R. Johnson. Dynamic analysis of a torsion specimen including heat conduction and plastic flow. *ASME J. Engng Mater. Technol.*, 103:201–206, 1981.

[72] A. B. Shapiro. TOPAZ3D—a three dimensional finite element heat transfer code. Tech. Rep. UCID-20484, Lawrence Livermore National Laboratory, 1985.

[73] G. R. Johnson and W. H. Cook. Fracture characteristics of three metals subjected to various strains, strain rates, temperatures and pressures. *Engng Fract. Mech.*, 21:31–48, 1985.

[74] N. J. Huffington, Jr. A reexamination of the plastic flow criterion for copper. To be published in *Proc. Army Symp. on Solid Mechanics*, 1991.

[75] P. S. Follansbee. Comparison between the rate and temperature dependent plasticity models of Bammann and of Kocks and Mecking. Tech. Rep. LA-11588-MS, Los Alamos National Laboratory, 1989.

[76] Douglas J. Bammann and Elias C. Aifantis. A model for finite deformation plasticity. *Acta Mech.*, 69:97–117, 1987.

[77] Douglas J. Bammann. A micro-mechanically motivated model of finite deformation plasticity. To be published, 1990.

[78] S. Nemat-Nasser. Rate-independent finite-deformation elastoplasticity: A new explicit constitutive algorithm. To be published, 1991.

[79] S. Nemat-Nasser and D. T. Chung. An explicit constitutive algorithm for large-strain, large-strain-rate elastic-viscoplasticity. To be published, 1991.

[80] S. Nemat-Nasser, D. T. Chung, and L. M. Taylor. Phenomenological modelling of rate dependent plasticity for high strain rate problems. *Mech. Mater.*, 7:319–344, 1989.

[81] John K. Dienes. Theory of deformation: Part I, kinematics. Report LA-11063-MS, Los Alamos National Laboratory, 1987.

[82] John K. Dienes. Theory of deformation: Part II, physical theory. Report LA-11063-MS, Los Alamos National Laboratory, 1989.

[83] Rodney J. Clifton. High strain rate behavior of metals. *Appl. Mech. Revs*, 43(5):S9–S22, 1990. Supplement, Part 2.

[84] K. A. Hartley, J. Duffy, and R. H. Hawley. Measurement of the temperature profile during shear band formation in steels deforming at high strain rates. *J. Mech. Phys. Solids*, 35(3):283–301, 1987.

[85] Ulrich S. Lindholm, A. Nagy, G. R. Johnson, and J. M. Hoegfeldt. Large strain, high strain rate testing of copper. *ASME J. Engny Mater. Technol.*, 102:376–381, 1980.

[86] Thomas W. Wright and John W. Walter, Jr. On stress collapse in adiabatic shear bands. *J. Mech. Phys. Solids*, 35(6):701–720, 1987.

[87] Thomas W. Wright and John W. Walter, Jr. Adiabatic shear bands in one dimension. In J. Harding, editor, *Mechanical Properties of Materials at High Rates of Strain 1989*, number 102 in Institute of Physics Conference Series, pages 119–126. Institute of Physics, Bristol and New York, 1989.

[88] Thomas W. Wright. Shear band susceptibility: Work hardening materials. To appear in *International Journal of Plasticity*, 1992.

[89] A. Marchand and J. Duffy. An experimental study of the formation process of adiabatic shear bands in a structural steel. *J. Mech. Phys. Solids*, 36(3):251–283, 1988.

[90] Lalit Anand, K. H. Kim, and Tarek G. Shawki. Onset of shear localization in viscoplastic solids. *J. Mech. Phys. Solids*, 35:407–429, 1987.

[91] Lalit Anand, A. M. Lush, and K. H. Kim. Thermal aspects of shear localization in viscoplastic solids. In M. H. Attia and L. Kops, editors, *Thermal Aspects in Manufacturing*, volume 30 of *PED*, pages 89–103. Am. Soc. Mech. Engr., 1988.

[92] Thomas W. Wright. Approximate analysis for the formation of adiabatic shear bands. *J. Mech. Phys. Solids*, 38(4):515–530, 1990.

[93] Thomas W. Wright. Adiabatic shear bands. *Appl. Mech. Revs*, 43(5):S196–S200, 1990. Supplement, Part 2.

[94] John W. Walter, Jr. Numerical experiments on adiabatic shear band formation in one dimension. Submitted to *International Journal of Plasticity*, 1991.

[95] Romesh C. Batra and Thomas W. Wright. A comparison of solutions for adiabatic shear banding by forward-difference and Crank-Nicolson methods. *Communs. Appl. Numer. Meths*, 4:741–748, 1988.

[96] Romesh C. Batra. The initiation and growth of, and the interaction among adiabatic shear bands in simple and dipolar materials. *Int. J. Plast.*, 3:75–89, 1987.

[97] Romesh C. Batra and C. H. Kim. On the interaction among adiabatic shear bands. In W. Soedel and J. F. Hamilton, editors, *Developments in Mechanics*, pages 117–122. Purdue University, 1987.

[98] Romesh C. Batra and C. H. Kim. Effect of material characteristic length on the initiation, growth, and band width of adiabatic shear bands in dipolar materials. *J. Phys. (Paris)*, 49:41–46, 1988.

[99] Romesh C. Batra. Effect of nominal strain rates on adiabatic shear banding in dipolar materials. In *Proceedings of the Pan American Congress of Applied Mechanics*, pages 79–82, Rio de Janiero, 1989.

[100] Messaoud Benantar, Rupak Biswas, Joseph E. Flaherty, and Mark S. Shephard. Parallel computation with adaptive methods for elliptic and hyperbolic systems. *Comput. Meth. Appl. Mech. Engng*, 82:73–93, 1990.

[101] Gerald L. Moss. Shear strains, strain rates, and temperature changes in adiabatic shear bands. Tech. Rep. ARBRL-TR-2242, U. S. Army Ballistic Research Laboratory, Aberdeen Proving Ground, MD 21005-5066, May 1980.

[102] Martin N. Raftenberg and Claire D. Krause. RHA plate perforation by a shaped-charge jet; experiment and simulation. In *Proceedings of the International Conference on Shock-Wave and High-Strain-Rate Phenomena in Materials*. Marcel Dekker, 1991. to appear.

[103] Gordon R. Johnson and R. A. Stryk. User instruction manual for the EPIC-2 code. Tech. Rep. AFATL-TR-86-51, Air Force Armament Laboratory, 1986.

[104] F. P. Stecher and Gordon R. Johnson. Lagrangian computations for projectile penetration into thick plates. In W. A. Gruver, editor, *Computers in Engineering 1984—Volume Two*, pages 292–299. Am. Soc. Mech. Engr., 1984.

[105] Donald R. Curran. Dynamic fracture. In J. A. Zukas, editor, *Impact Dynamics*, pages 333–366. Wiley, 1982.

[106] Lynn Seaman and Donald R. Curran. Development of a model for shear banding: SHEAR3. Contr. Rep. BRL-CR-590, U. S. Army Ballistic Research Laboratory, Aberdeen Proving Ground, MD 21005-5066, 1987.

[107] Lynn Seaman, T. Cooper, and D. Erlich. User's manual for C-HEMP, a two-dimensional wave propagation code. Volume I: Description and derivations of the code. Contr. Rep. BRL-CR-587, U. S. Army Ballistic Research Laboratory, Aberdeen Proving Ground, MD 21005-5066, 1987.

[108] J. O. Hallquist. User's manual for DYNA2D—an explicit two-dimensional hydrodynamic finite element code with interactive rezoning (rev. 2). Tech. Rep. UCID-18756, Lawrence Livermore Laboratory, January 1984.

[109] Donald R. Curran, 1990. Private communication with M. Raftenberg.

[110] D. A. Shockey *et al.* Failure phenomenology of confined ceramic targets and impacting rods. *Int. J. Impact Engng*, 9:263–275, 1990.

[111] Sia Nemat-Nasser and M. Horii. Void collapse and void growth in crystalline solids. *J. Appl. Phys.*, 62:2746–2757, 1986.

[112] M. Horii and Sia Nemat-Nasser. Brittle failure in compression: Splitting, faulting and brittle-ductile transition. *Phil. Trans. R. Soc. Lond.* A, 319:337–374, 1987.

[113] M. F. Ashby and S. D. Hallam. The failure of brittle solids containing small cracks under compressive stress states. *Acta Metall.*, 34:497–510, 1986.

[114] C. G. Sammis and M. F. Asby. The failure of brittle porous solids under compressive stress states. *Act. Metall.*, 34:511–526, 1986.

[115] L. H. L. Louro and M. A. Meyers. Effect of stress state and microstructural parameters on impact damage of alumina-based ceramics. *J. Mater. Sci.*, 24:2516–2532, 1989.

[116] J. Lankford. Temperature-strain rate dependence of compressive strength and damage mechanisms in aluminum oxide. *J. Mater. Sci.*, 16:1567–1578, 1981.

[117] J. Cagnoux. Spherical waves in pure alumina. Effects of grain size on flow and fracture. Conference proceedings.

[118] J. Lankford. Mechanisms responsible for strain-rate-dependent compressive strength in ceramic materials. *Communs. Am. Cer. Soc.*, pages C33–C34, 1981.

[119] M. E. Kipp, D. E. Grady, and E. P. Chen. Strain-rate dependent fracture initiation. *Int. J. Fract. Mech.*, 16:471–478, 1980.

[120] D. E. Grady and M. E. Kipp. Fragmentation of solids under dynamic loading. In T. Wierzbicki *et al.*, editors, *Structural Failure*, pages 1–40. Wiley, 1989.

[121] L. B. Freund. *Dynamic Fracture Mechanics.* Cambridge University Press, 1990.

[122] D. E. Grady. The spall strength of condensed matter. *J. Mech. Phys. Solids*, 36:353–384, 1988.

[123] D. A. Shockey, D. C. Erlich, J. F. Kalthoff, and H. Homma. Short-pulse fracture mechanics. *Engng Fract. Mech.*, 23:311–319, 1986.

[124] M. Kachanov, E.L.E. Montagut, and J.P. Laures. Mechanics of crack-microcrack interactions. *Mech. Mater.*, 10:59–71, 1990.

[125] F. Longy and J. Cagnoux. Macro and micro-mechanical aspects of shock loading of aluminas. In C. Y. Chiem *et al.*, editors, *Impact Loading and Dynamic Behavior of Materials*, volume 1, pages 1001–1008. 1988.

[126] D. Yaziv, Y. Yeshurun, Y. Partom, and Z. Rosenberg. Shock structure and precursor decay in commercial alumina. In S. C. Schmidt *et al.*, editors, *Shock Waves in Condensed Matter*, pages 297–300. Elsevier, 1988.

[127] Z. Rosenberg, D. Yaziv, Y. Yeshurun, and S. J. Bless. Shear strength of shock-loaded alumina as determined with longitudinal and transverse manganin gauges. *J. Appl. Phys.*, pages 1120–1122, 1987.

[128] D. J. Steinberg. Computer studies of the dynamic strength of ceramics. Tech. Rep. UCRL-ID-106004, Lawrence Livermore National Laboratory, 1990.

[129] J. R. Furlong, M. L. Alme, and J.F. Davis. Modeling the dynamic load/unload behavior of ceramics under impact loading. Tech. Rep. RDA-TR-0030-0001-001, R&D Associates, 1990.

[130] S. Segletes. Trip report: 7th ceramic modeling working group meeting. Prepared for the USABRL, April 1991.

[131] D. R. Curran, L. Seaman, and D.A. Shockey. Dynamic failure of solids. *Phys. Rep.*, 147(5-6):253–388, 1987.

[132] F. L. Addessio and J. N. Johnson. A constitutive model for the dynamic response of brittle materials. *J. Appl. Phys.*, 67:3275–3286, 1990.

[133] D. E. Grady, 1991. Personal communication to S. Segletes of USABRL, APG, MD.

[134] Michael J. Scheidler. Trip report: 8th ceramic modeling working group meeting. Prepared for the USABRL, December 1991.

[135] S. Segletes. Modeling improvements: The post-failure hydrostatic behavior of brittle materials, May 1990. Presented at the Conference on the Application of 3-D Hydrocodes to Armor/Anti-Armor Problems, APG, MD.

[136] D. R. Curran, L. Seaman, and T. Cooper. Micromechanical model for deformation of aggregates of fragments, grains, or blocks: Application to penetration of ceramic armor. Draft report, Stanford Research Inst. Intl., 1991.

[137] R. Scott. Constitutive relations for soil: Present and future. In A. Saada and G. Bianchini, editors, *Constitutive Equations for Granular Non-Cohesive Soils*, pages 723–725. A. A. Balkema, Rotterdam, 1988.

[138] Sia Nemat-Nasser. Fourth annual on-site review of the URI center for ultradynamic performance materials. Univ. of Calif. San Diego report, March 1991.

[139] J. Jenkins, September 1990. Invited presentation at the USABRL, APG, MD.

[140] Steven B. Segletes. Thermodynamic stability of the Mie-Grueneisen equation of state, and its relevance to hydrocode computations. *J. Appl. Phys.*, 70(5), 1991.

[141] D. A. Matuska and J. J. Osborn. *HULL Technical Manual, Volume II.* Orlando Technology Incorporated, 1986.

[142] D. A. Matuska, J. J. Osborn, and E. W. Piburn. *HULL Documentation Volume I: Technical Discussion.* Orlando Technology Incorporated, August 1991.

[143] D. A. Matuska, J. J. Osborn, and E. W. Piburn. *HULL Documentation Volume II: Users Manual.* Orlando Technology Incorporated, August 1991.

[144] R. L. Bell *et al.* CTH user's manual and input instructions, version 1.023. Internal Report, Sandia National Laboratories, June 1991.

[145] J. H. Tillotson. Metallic equations of state for hypervelocity impact. Tech. Rep. GA-3216, General Atomics, July 1962. [AD486711].

[146] Thomas W. Wright and Konrad Frank. Approaches to penetration problems. In W. J. Ammann, W. K. Liu, J. A. Studer, and T. Zimmermann, editors, *Impact: Effects of Fast Transient Loadings.* Balkema, 1988.

[147] Romesh C. Batra and Z. G. Zhu. Dynamic shear band development in a thermally softening bimetallic body containing two voids. *Acta Mech.*, 86:31–52, 1991.

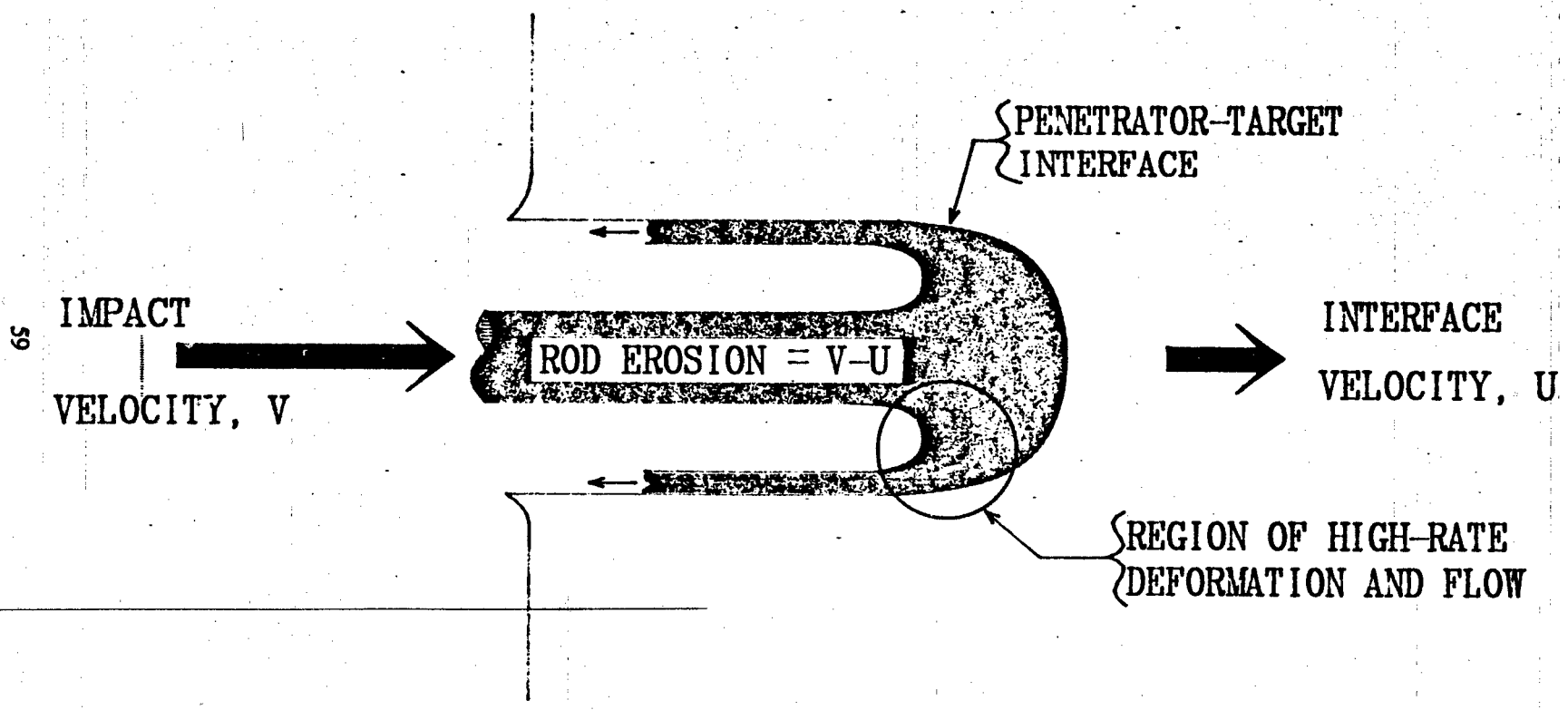

Figure 1. Hydrodynamic Idealization of the Penetration Process.

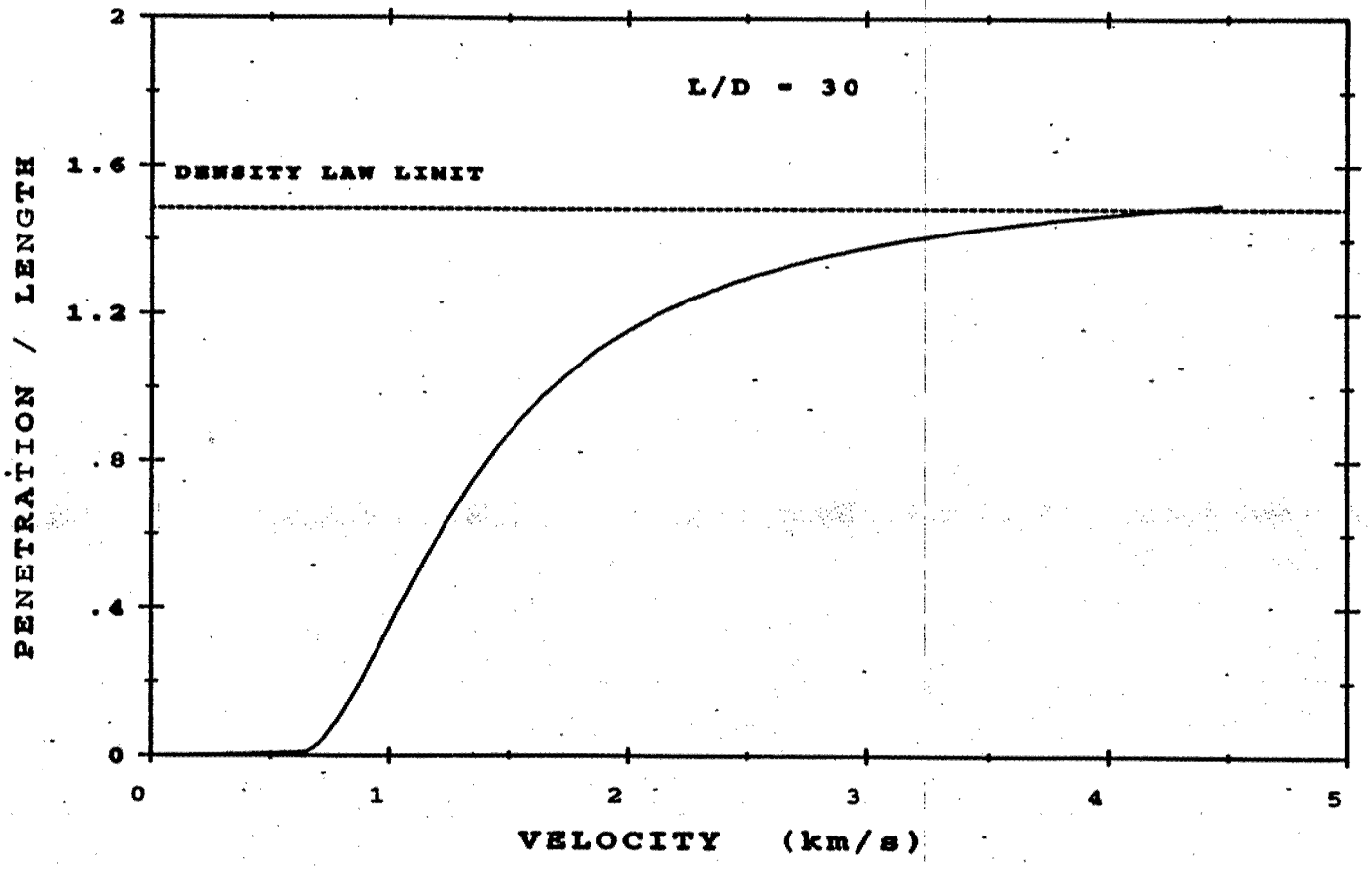

Figure 2. Penetration Prediction of Eroding-Rod Velocity Models.

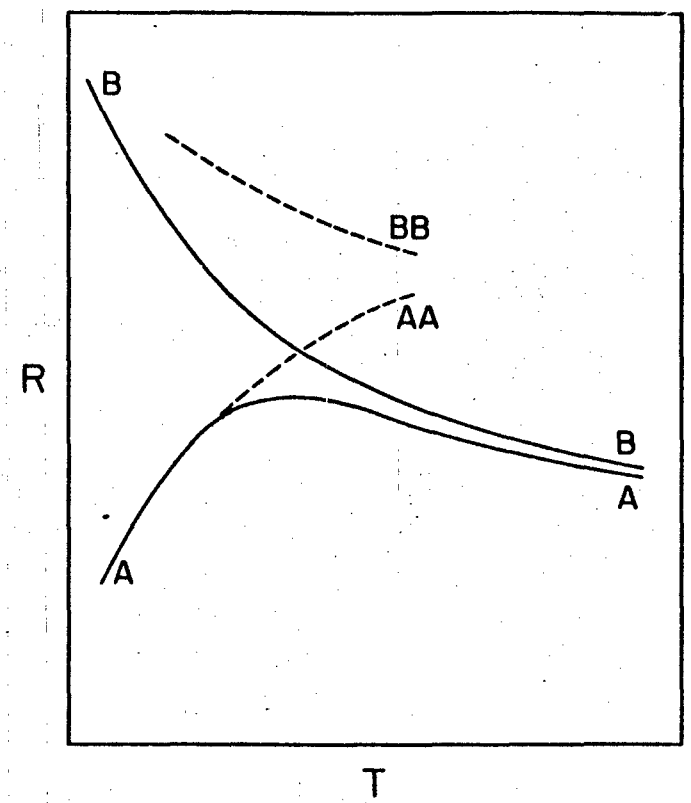

Figure 3. Performance Trends Determined by the Analysis of Penetration Into Ceramic-Laminate Targets.

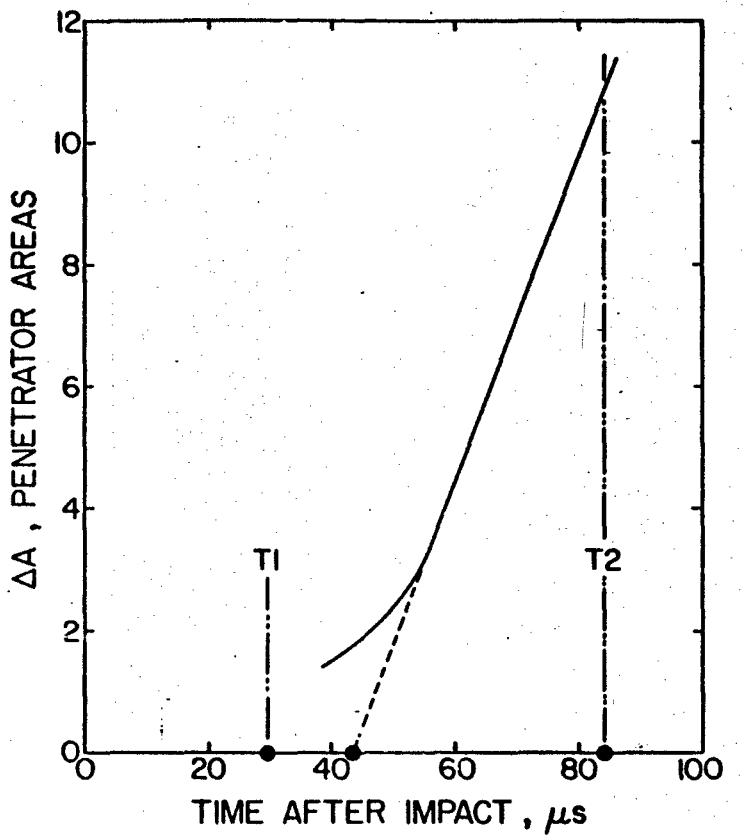

Figure 4. Increase in Target Area as a Function of Time.

Figure 5. Orthogonal Post-Test Radiographs Showing a Penetration Path Modified by Planar Failure that Resulted From Wave Interactions.

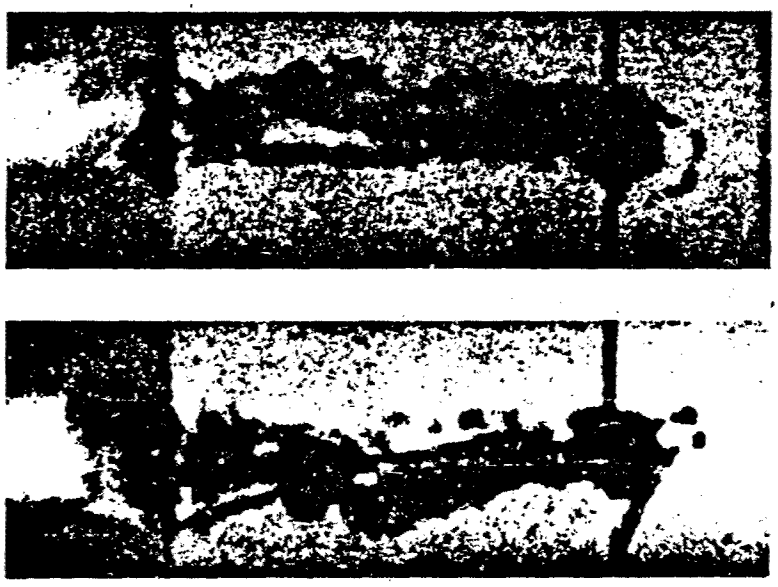

Figure 6. Orthogonal Post-Test Radiographs Showing a Symmetrical Penetration Path Achieved by Installing Wave Traps at the Side Boundaries.

Figure 7. Orthogonal Failure Planes and Radial Cracks in a Recovered Ceramic Target Without Wave Traps.

Figure 8. A Shear Band Near the Hole in an RHA Plate Perforated by a Copper Shaped-Charge Jet. SEM Micrograph; 3700x Mag., 2% Nital Etch.

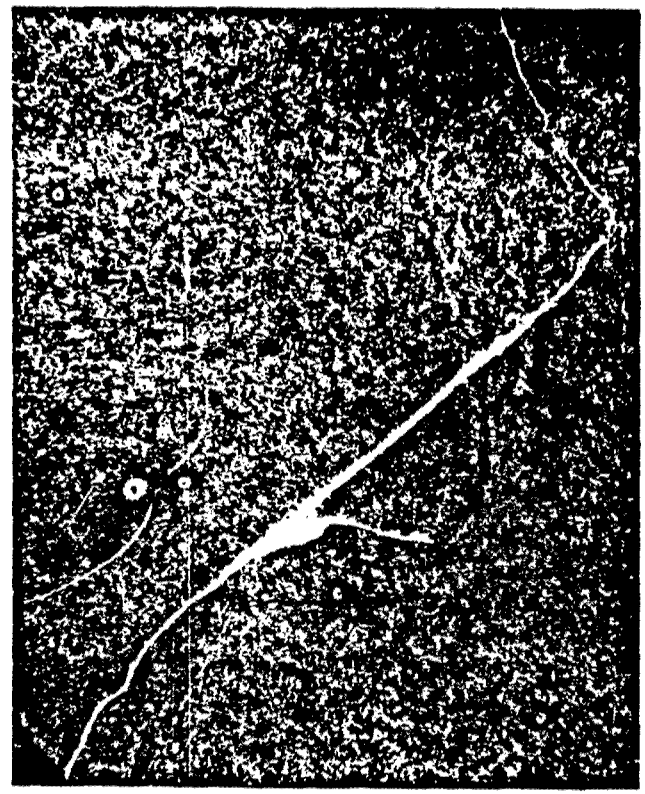

Figure 9. A Sheer Band in an RHA Fragment From a Plate Perforated by a Copper Shaped-Charge Jet. Photomicrograph; 80x Mag.; 2% Nital Etch.

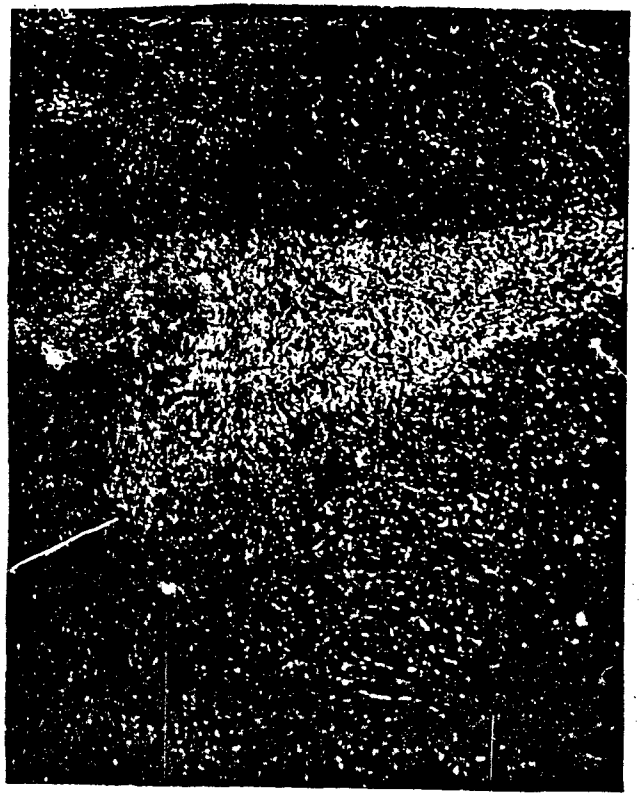

Figure 10. Enlargement of the Shear Band in Figure 9. Photomicrograph; 625x Mag.; 2% Nital Etch.

Figure 11. An RHA Fragment With a White-Etching Boundary Region. Fragment is From a Plate Perforated by a Copper Shaped-Charge Jet. Photomicrograph; 100x Mag.; 2% Nital Etch.

Figure 12. A Crack That Runs Along a Shear Band in an RHA Plate Perforated by a Copper Shaped-Charge Jet. Photomicrograph; 800x Mag.; 2% Nital Etch.

Figure 13. The Crack in Figure 12 Emanates From the Hole Boundary on the Plate. Photomicrograph; 80x Mag.; 2% Nital Etch.

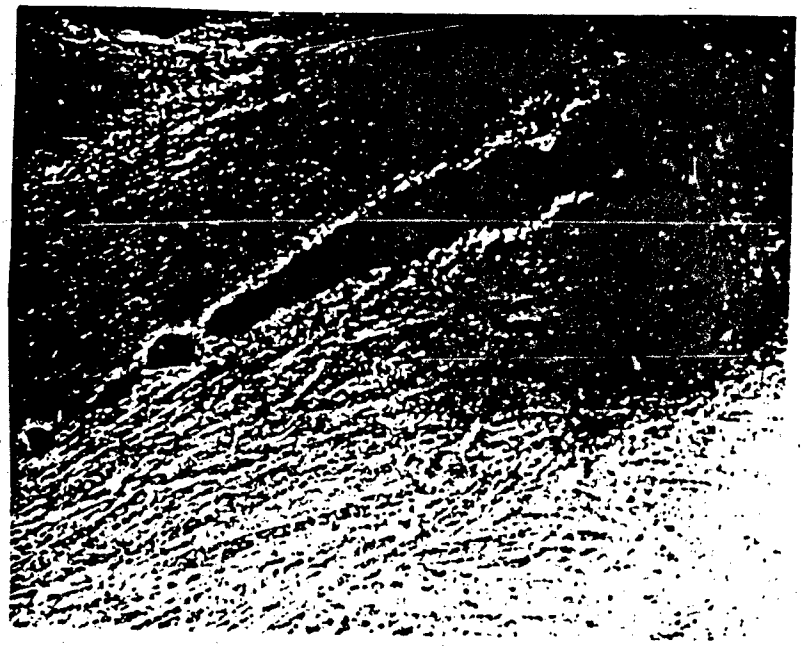

Figure 14. Voids Have Coalesced to Form a Crack in an RHA Plate Perforated by a Copper Shaped-Charge Jet. SEM Micrograph; 4,000x Mag.; 2% Nital Etch.

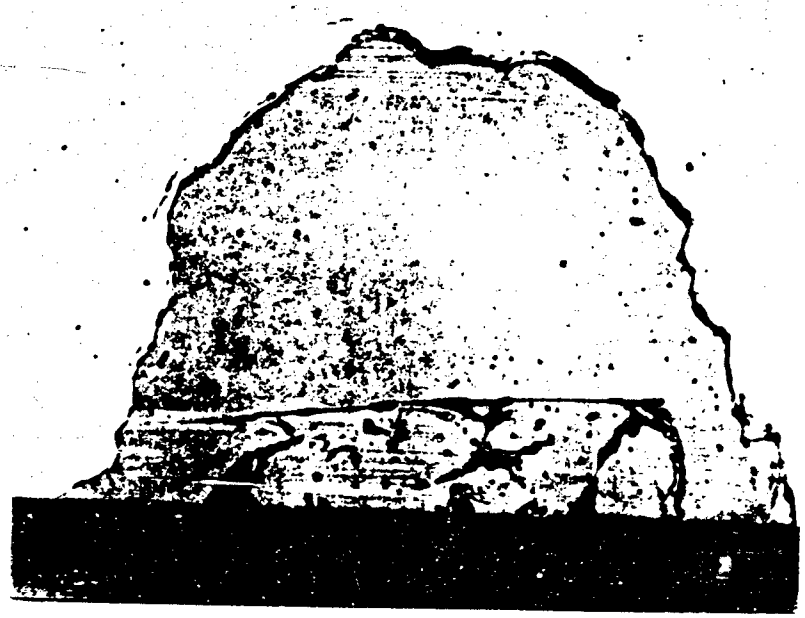

Figure 15. U-3/4% Ti Penetrator Remnant Unbedded in Steel Armor.

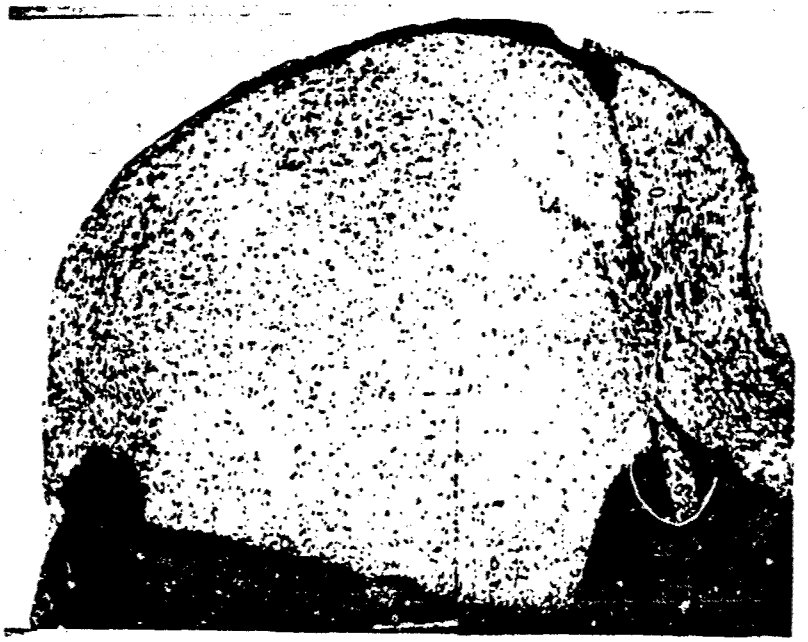

Figure 16. WHA Penetrator Embedded in Steel Armor.

Figure 17. Behind-Armor Radiograph Showing Mushroomed Nose of WHA Residual Penetrator.

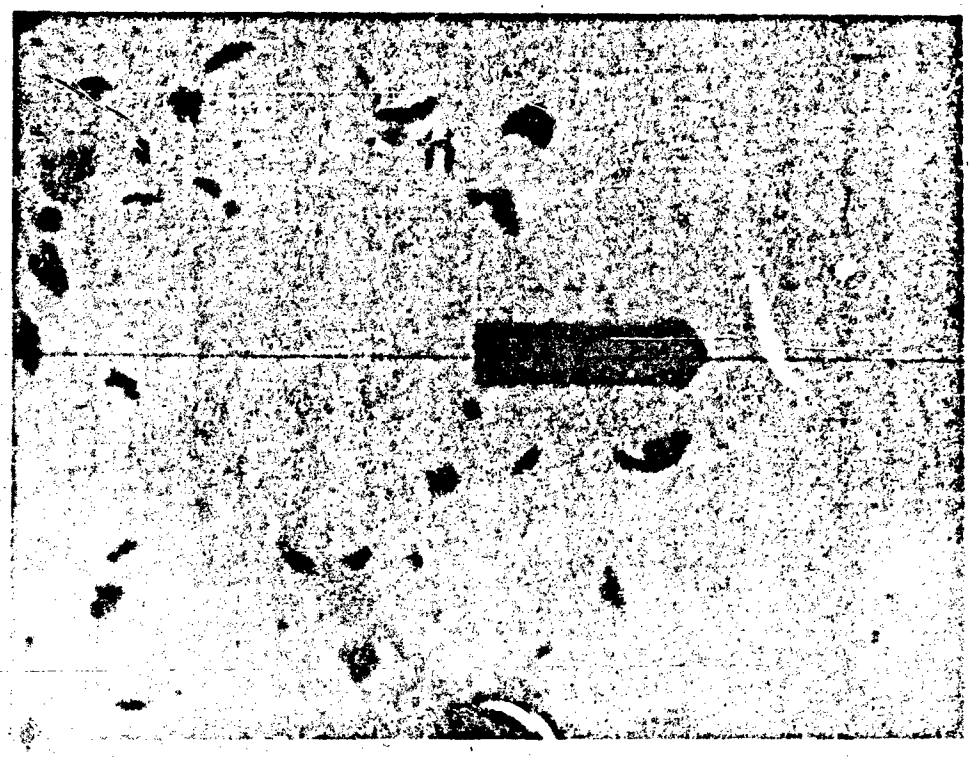

Figure 18. Behind-Armor Radiograph Showing Chiselled Nose of Uranium Residual Penetrator.

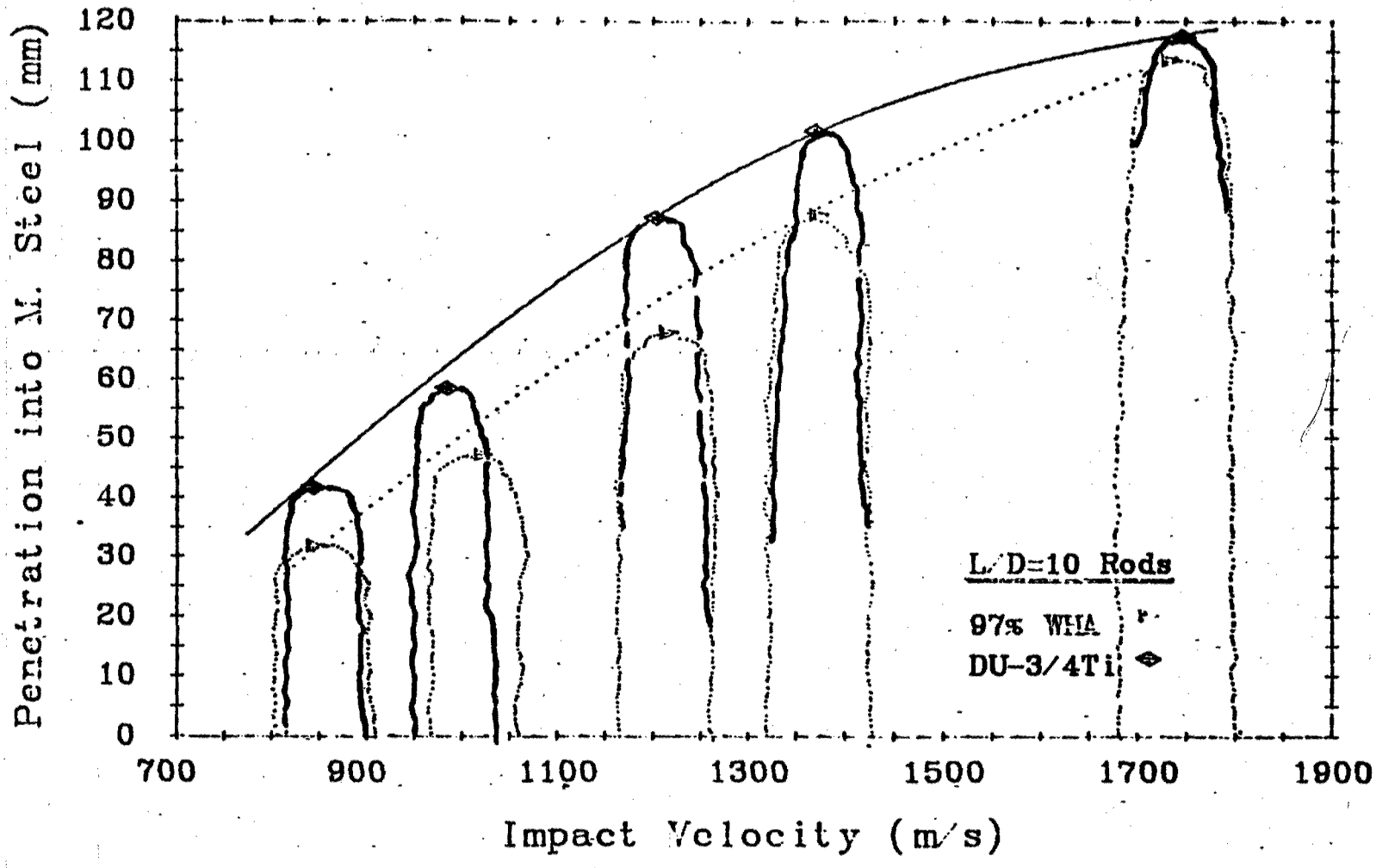

Figure 19. Depth of Penetration and Penetration Tunnel Profiles - DU and 97% WHA Into Mild Steel.

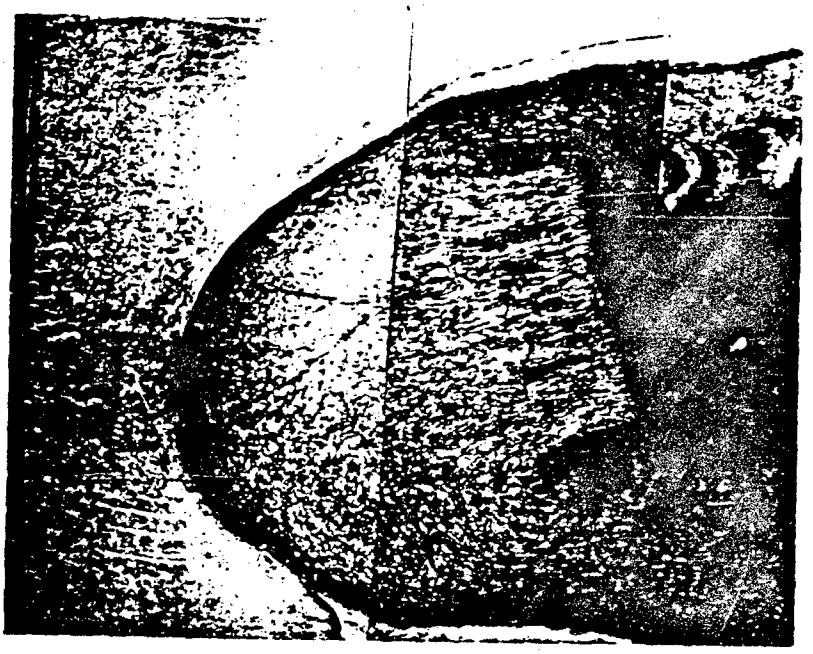

Figure 20. Extreme Bulk Deformation (Mushrooming) of Polycrystal W Penetrator.

Figure 21. Semi-Infinite Residual Penetrator Section for the [110] Orientation. Photomicrograph; 10x Mag.; As Polished.

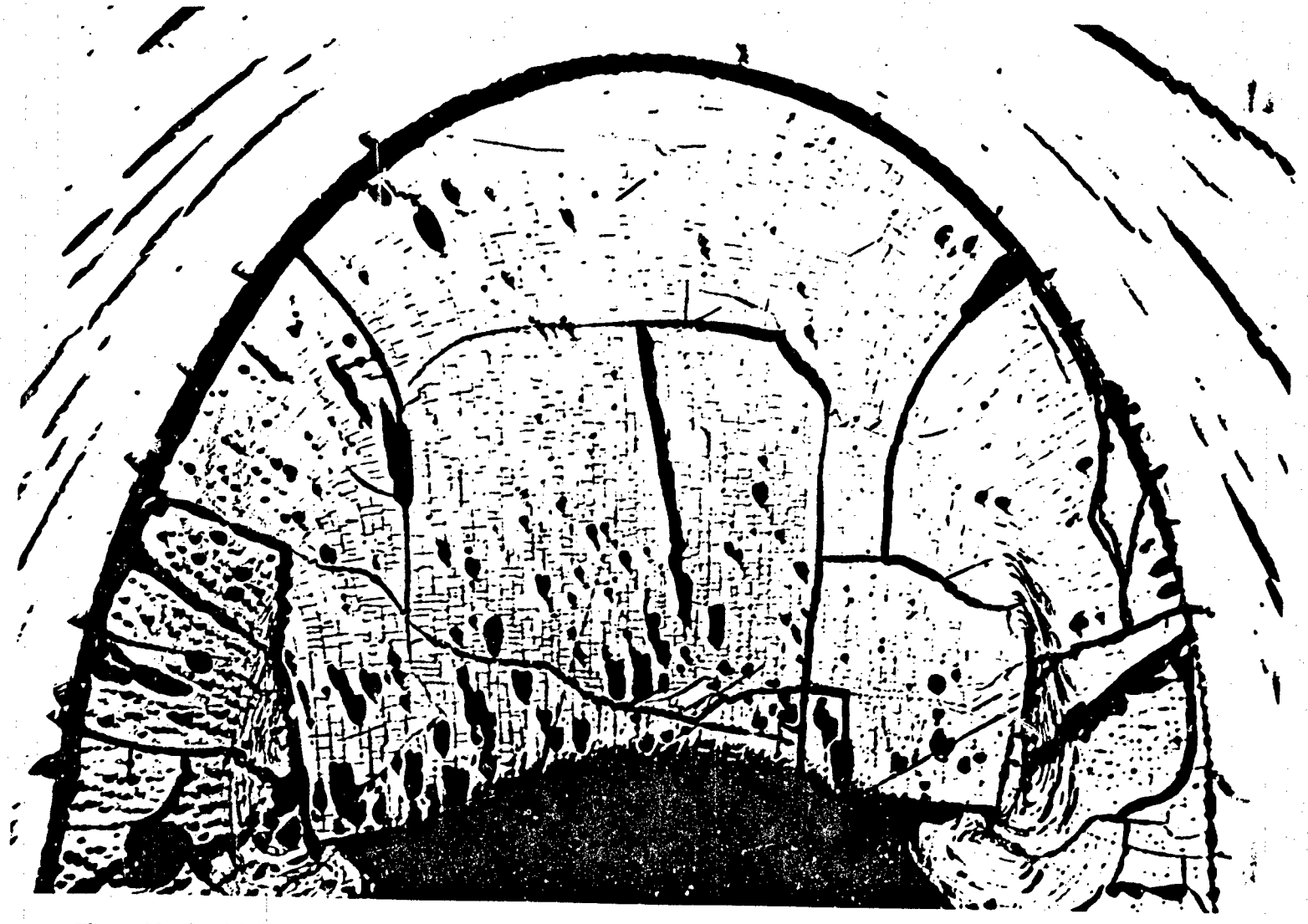

Figure 22. Semi-Infinite Residual Penetrator Section for the [100] Orientation. Photomicrograph; 10x Mag.; As Polished.

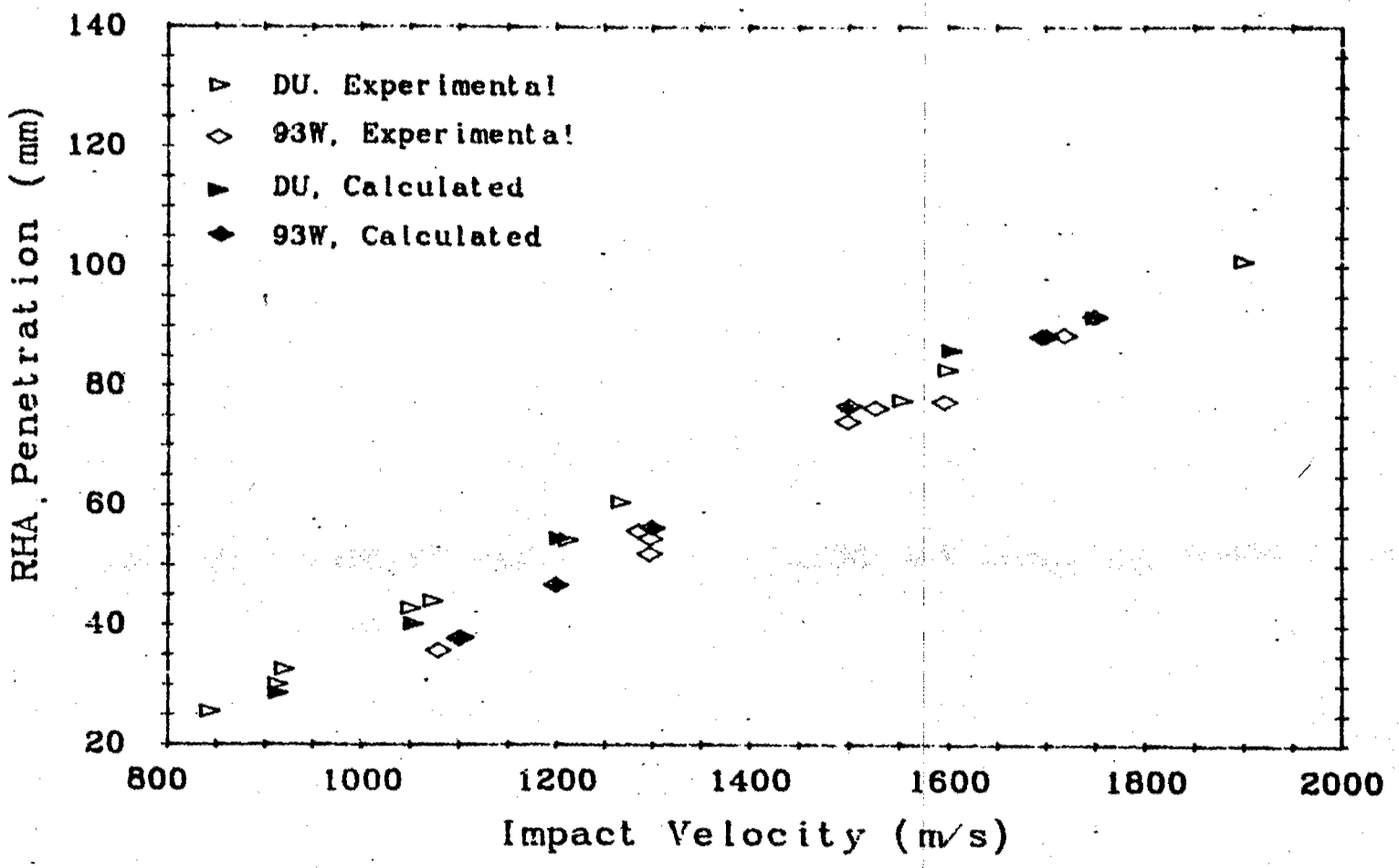

Figure 23. Semi-Infinite Penetration of U-3/4% Ti vs. 93% W (Constant 65-g Mass Penetrators, L/D=10).

No. of Copies	Organization
2	Administrator Defense Technical Info Center ATTN: DTIC-DDA Cameron Station Alexandria, VA 22304-6145
1	Commander U.S. Army Materiel Command ATTN: AMCAM 5001 Eisenhower Ave. Alexandria, VA 22333-0001
1	Commander U.S. Army Laboratory Command ATTN: AMSLC-DL 2800 Powder Mill Rd. Adelphi, MD 20783-1145
2	Commander U.S. Army Armament Research, Development, and Engineering Center ATTN: SMCAR-IMI-I Picatinny Arsenal, NJ 07806-5000
2	Commander U.S. Army Armament Research, Development, and Engineering Center ATTN: SMCAR-TDC Picatinny Arsenal, NJ 07806-5000
1	Director Benet Weapons Laboratory U.S. Army Armament Research, Development, and Engineering Center ATTN: SMCAR-CCB-TL Watervliet, NY 12189-4050
(Unclass. only) 1	Commander U.S. Army Rock Island Arsenal ATTN: SMCRI-TL/Technical Library Rock Island, IL 61299-5000
1	Director U.S. Army Aviation Research and Technology Activity ATTN: SAVRT-R (Library) M/S 219-3 Ames Research Center Moffett Field, CA 94035-1000
1	Commander U.S. Army Missile Command ATTN: AMSMI-RD-CS-R (DOC) Redstone Arsenal, AL 35898-5010

No. of Copies	Organization
1	Commander U.S. Army Tank-Automotive Command ATTN: ASQNC-TAC-DIT (Technical Information Center) Warren, MI 48397-5000
1	Director U.S. Army TRADOC Analysis Command ATTN: ATRC-WSR White Sands Missile Range, NM 88002-5502
1	Commandant U.S. Army Field Artillery School ATTN: ATSF-CSI Ft. Sill, OK 73503-5000
(Class. only) 1	Commandant U.S. Army Infantry School ATTN: ATSH-CD (Security Mgr.) Fort Benning, GA 31905-5660
(Unclass. only) 1	Commandant U.S. Army Infantry School ATTN: ATSH-CD-CSO-OR Fort Benning, GA 31905-5660
1	WL/MNOI Eglin AFB, FL 32542-5000
	Aberdeen Proving Ground
2	Dir, USAMSAA ATTN: AMXSY-D AMXSY-MP, H. Cohen
1	Cdr, USATECOM ATTN: AMSTE-TC
3	Cdr, CRDEC, AMCCOM ATTN: SMCCR-RSP-A SMCCR-MU SMCCR-MSI
1	Dir, VLAMO ATTN: AMSLC-VL-D
10	Dir, USABRL ATTN: SLCBR-DD-T

No. of Copies	Organization
7	Director U.S. Army Research Office ATTN: J. Chandra K. Clark J. Wu K. Iyer B. Henriksen A. Crowson Technical Library P.O. Box 1211 Research Triangle Park, NC 27709-2211
1	Commander U.S. Army Research and Standardization Group (Europe) ATTN: F. Oertel P.O. Box 65 FPO NY 09510
1	Director U.S. Army Materials Technology Laboratory ATTN: SLCMT-D Watertown, MA 02172-0001
1	Director U.S. Army Materials Technology Laboratory ATTN: SLCMT-MR, G. Bishop Watertown, MA 02172-0001
6	Director U.S. Army Materials Technology Laboratory ATTN: SLCMT-MRD, S. Chou J. Dandekar A. Rajendran T. Weerasooriya C. White P. Woolsey Watertown, MA 02172-0001
2	Director U.S. Army Materials Technology Laboratory ATTN: SLCMT-EMC, J. Beatty M. Slavin Watertown, MA 02172-0001

No. of Copies	Organization
1	Commander U.S. Army Tank-Automotive Command ATTN: AMSTA-RSK, J. Thompson Warren, MI 48397-5000
1	U.S. Naval Academy Department of Mathematics ATTN: R. Malek-Madani Annapolis, MD 21402
1	Air Force Wright Aeronautical Laboratories Air Force Systems Command Materials Laboratory ATTN: T. Nicholas Wright-Patterson AFB, OH 45433
7	Commander U.S. Army Armament Research, Development, and Engineering Center ATTN: SMCAR-AEE-WW, E. Baker SMCAR-AET, B. Bushey W. Ebihara SMCAR-AET-M, F. Witt S. Cytron D. Kapoor K. Willison Picatinny Arsenal, NJ 07806-5000
1	Commander U.S. Army Armament Research, Development, and Engineering Center ATTN: SMCAR-TDS, V. Lindler Picatinny Arsenal, NJ 07806-5000
2	Commander U.S. Army Belvoir Research, Development, and Engineering Center ATTN: STRBE, S. Bishop STRBE-N, D. Heberlein Fort Belvoir, VA 22060

No. of Copies	Organization
2	Director U.S. Army Engineer Waterways Experiment Station ATTN: CEWES-SD, J. G. Jackson B. Bohani 3909 Halls Ferry Road Vicksburg, MS 39180-6199
1	Commander U.S. Army Laboratory Command ATTN: AMSLC-TD, R. Vitali 2800 Powder Mill Road Adelphi, MD 20783-1145
2	Commander U.S. Army Missile Command ATTN: AMSMI-RD, W. Jennings, Jr. AMSMI-RD-ST-WF, M. Schexnayder Redstone Arsenal, AL 35898
1	Commander U.S. Army Tank-Automotive Command Armor Application Section ATTN: AMSTA-RSK, S. Goodman Warren, MI 48397-5000
3	Director U.S. Air Force Armament Technology Laboratory ATTN: AD/MNW, J. Foster J. Collins B. Cook Eglin Air Force Base, FL 32542-5434
1	Director U.S. Air Force Armament Technology Laboratory ATTN: CA, S. Lambert Eglin Air Force Base, FL 32542-5434
1	Director U.S. Air Force Weapons Laboratory ATTN: NTI, Charles Mulligan Kirtland Air Force Base, NM 87185

No. of Copies	Organization
5	Commander Naval Weapons Center ATTN: Code 3266, R. Hoffmann Code 3261, T. Gill R. Lundstrom Code 32, D. Goss Code 3205, F. Markarian China Lake, CA 93555-6001
4	Commander Naval Surface Warfare Center ATTN: Code R10, L. Roslund Code R12, P. Walter L. Hudson H. Mair Silver Spring, MD 20903-5000
1	Commander Naval Surface Warfare Center ATTN: Code G06, D. Brunson Dahlgren, VA 22448-5000
1	Director Defense Advanced Research Projects Agency ATTN: J. Richardson Armor/Antiarmor Joint Program Office Rosslyn, VA 22209-2308
2	Director Defense Advanced Research Projects Agency ATTN: B. Wilcox Tech. Info. 3701 North Fairfax Dr. Arlington, VA 22203-1714
1	Director Defense Advanced Research Projects Agency Land Systems Office ATTN: T. Phillips 3701 North Fairfax Dr. Arlington, VA 22203-1714

No. of Copies | Organization

1 Director
Defense Nuclear Agency
ATTN: DNA/SPSD, M. Giltrud
6801 Telegraph Road
Alexandria, VA 22310-3398

1 Office of Munitions
ATTN: OUSD(A)/TWD/OM, A. Holt
Room 3B1060, The Pentagon
Washington, DC 20301

1 Commander
Naval Postgraduate School
ATTN: Code 73, J. Sternberg
Monterey, CA 93943

1 Commander
MCRDAC
ATTN: Code AW, D. Vaughn
Quantico, VA 22134-5080

5 Director
Sandia National Laboratories
ATTN: Div 1543,
D. Grady
M. Kipp
W. Herrman
S. Passman
M. Forrestal
P.O. Box 5800
Albuquerque, NM 87185-5800

1 Director
Sandia National Laboratories
ATTN: D. Bammann
Livermore, CA 94550

1 National Institute of Science and Technology
ATTN: T. Burns
Technology Building, Rm A151
Gaithersburg, MD 20899

1 Director
U.S. Department of Energy
ATTN: DP 242, GTN, R&AT/OMA,
G. D'Alessio
Washington, DC 20545

No. of Copies | Organization

9 Director
Lawrence Livermore National Laboratory
ATTN: L-11, M. Finger
MS L-35,
R. Christensen
R. Couch
R. Tipton
D. Baum
D. Steinberg
MS L-321, J. Reaugh
MS L342, D. Lassila
C. Cline
P.O. Box 808
Livermore, Ca 94550

5 Director
Los Alamos National Laboratory
ATTN: MS K574,
E. Cort
R. Gates
B. Hogan
P. Howe
S. Skaggs
Los Alamos, NM 87454

7 Director
Los Alamos National Laboratory
ATTN: MS F663,
J. Johnson
R. Karpp
S. Shiferl
T. Adams
D. Mandell
P. Follansbee
J. Hopson
Los Alamos, NM 87454

6 Director
Los Alamos National Laboratory
ATTN: MS B216, F. Addessio
MS B221,
D. Tonks
J. Dienes
MS B295, K. Holian
MS E546, W. Blumenthal
MS K557, R. Henninger
Los Alamos, NM 87454

No. of Copies	Organization
9	Director Los Alamos National Laboratory ATTN: MS J576, M. Lewis D. Rabern MS F664, L. Schwalbe MS F668, F. Day MS F669, J. Repa MS G771, F. Gac MS G787, M. Burkett MS J960, L. Hull J. Straight Los Alamos, NM 87454
7	Director Sandia National Laboratories ATTN: Div 1420, B. Camp Div 1533, P. Yarrington Div 9123, J. Hitchcock J. McGlaun E. Hertel V. Luk D. Gardner P.O. Box 5800 Albuquerque, NM 87185
2	Brown University Division of Engineering ATTN: R. Clifton B. Freund Providence, RI 02912
1	University of California at Santa Barbara Department of Materials Science ATTN: A. Evans Santa Barbara, CA 93106
4	University of California at San Diego Department of Applied Mechanics and Engineering Sciences ATTN: R. Asaro G. Hegemeier M. Meyers S. Nemat-Nasser La Jolla, Ca 92093
2	California Institute of Technology ATTN: W. Knauss G. Ravichandran Mail Code 105-50 Pasadena, CA 91125
1	Carnegie-Mellon University Department of Mathematics ATTN: M. Gurtin Pittsburgh, PA 15213
1	University of Cincinnati Department of Mathematical Sciences ATTN: D. French Old Chemistry Building (ML 25) Cincinnati, OH 45221
1	Cornell University Department of Theoretical and Applied Mechanics ATTN: J. Jenkins Ithaca, NY 14850
2	Drexel University Department of Materials Engineering ATTN: H. Rogers P. Chou Philadelphia, PA 18104
1	Harvard University Division of Engineering and Applied Physics ATTN: J. Hutchinson Cambridge, MA 02138
2	University of Illinois Department of Theoretical and Applied Mechanics ATTN: D. Carlson T. Shawki Urbana, IL 61801
1	University of Illinois at Chicago Circle Department of Engineering, Mechanics, and Metallurgy ATTN: T. Ting P.O. Box 4348 Chicago, IL 60680

No. of Copies	Organization
3	The Johns Hopkins University Department of Mechanical Engineering Latrobe Hall ATTN: A. Douglas K. Ramesh W. Sharp 34th and Charles Streets Baltimore, MD 21218
1	University of Kentucky Department of Engineering Mechanics ATTN: O. Dillon, Jr. Lexington, KY 40506
2	University of Maryland Department of Mechanical Engineering ATTN: R. Armstrong J. Dally College Park, MD 20742
1	University of Maryland Baltimore County ATTN: A. Khan Baltimore, MD 21228
1	Massachusetts Institute of Technology Department of Mechanical Engineering ATTN: L. Anand Cambridge, MA 02139
2	University of Minnesota Department of Aerospace Engineering and Mechanics ATTN: R. Fosdick R. James 110 Union Street SE Minneapolis, MN 55455
1	University of Missouri-Rolla Department of ME, AE & EM ATTN: R. Batra Rolla, MO 65401-0249
1	University of Nebraska Department of Engineering Mechanics ATTN: M. Beatty 212 Bancroft Hall Lincoln, NE 68588

No. of Copies	Organization
3	State University of New York at Stony Brook Department of Applied Mathematics and Statistics ATTN: J. Glimm J. Grove B. Plohr Stony Brook, NY 11794
1	North Carolina State University Department of Civil Engineering ATTN: Y. Horie Raleigh, NC 27607
1	North Carolina State University Department of Mathematics ATTN: M. Shearer Raleigh, NC 27695
1	North Carolina State University Department of Mechanical and Aerospace Engineering ATTN: M. Zikry Raleigh, NC 27695
1	Northwestern University Department of Applied Mathematics ATTN: W. Olmstead Evanston, IL 60208
1	Northwestern University Department of Civil Engineering ATTN: T. Belytschko Evanston, IL 60208
1	Rensselaer Polytechnic Institute Department of Mechanical Engineering ATTN: E. Krempl Troy, NY 12181
1	Rensselaer Polytechnic Institute Department of Computer Science ATTN: J. Flaherty Troy, NY 12181
1	University of Texas Texas Institute for Comp. Mechanics ATTN: J. Oden Austin, TX 78712

No. of Copies	Organization
1	Texas A&M University Aerospace Engineering Department ATTN: T. Strouboulis College Station, TX 77843-3141
1	Washington State University Department of Physics ATTN: Y. Gupta Pullman, WA 99163
1	Washington State University Department of Mechanical and Materials Engineering ATTN: H. Zbib Pullman, WA 99164
1	Institute for Defense Analysis ATTN: G. Mayer 1801 N. Beauregard Street Alexandria, VA 22311
4	SRI International ATTN: D. Curran R. Shockey L. Seaman H. Giovanola 333 Ravenswood Avenue Menlo Park, CA 94025
3	Southwest Research Institute Department of Mechanical Sciences ATTN: C. Anderson J. Lankford U. Lindholm 8500 Culebra Road San Antonio, TX 02912
2	California Research and Technology, Inc. ATTN: D. Orphal P. Schneiwind 5117 Johnson Dr. Pleasanton, CA 94566
2	General Research Corporation ATTN: A. Charters T. Menna 5383 Hollister Ave. Santa Barbara, CA 93111

No. of Copies	Organization
2	Alliant Techsystems, Inc. ATTN: G. Johnson T. Holmquist 7225 Northland Dr. Brooklyn Park, MN 55428
1	Research & Development Associates ATTN: J. Furlong 2100 Washington Blvd. Arlington, VA 22209
1	Aluminum Company of America ATTN: R. Stemler ALCOA Center, PA 15069
1	E.I. DuPont de Nemours ATTN: M. Bernhardt P.O. Box 80702 Wilmington, DE 19898
1	General Dynamics Land Systems Division ATTN: W. Burke P.O. Box 1800 Warren, MI 48090
2	Kaman Sciences Corporation ATTN: J. May M. Normandia P.O. Box 7643 Colorado Springs, CO 80933
1	California Research and Technology, Inc. ARAP Group - A Titan Company ATTN: R. Thorpe P.O. Box 2229 Princeton, NJ 08543
1	Battelle Ordnance Systems and Technology Department ATTN: D. Butz 505 King Ave. Columbus, OH 43201-2693
2	Battelle ATTN: G. Dudder W. Gurwell P.O. Box 999 Richland, WA 99352

No. of Copies	Organization
1	Coors Ceramic Company ATTN: R. Paricio 600 Ninth St. Golden, CO 80401
1	DOW Chemical USA Ordnance Systems ATTN: K. Epstein 800 Building Midland, MI 48667
1	GTE Products Corporation Chemical and Metallurgical Division ATTN: J. Gonzalez Hawes St. Towanda, PA 18848
1	The Carborundum Company Structural Ceramics Division ATTN: M. Leitten 20422 Beach Blvd., Suite 315 Huntington Beach, CA 92648
1	Teledyne-Brown Engineering ATTN: L. Smalley, MS 50 P.O. Box 07007 Huntsville, AL 35807-7007
1	Failure Analysis Associates ATTN: S. Andrew P.O. Box 3015 Menlo Park, CA 94025
1	CERCOM, Inc. ATTN: R. Palicka P.O. Box 70 Buena Vista, CA 92083
2	Lanxide Armor Products, Inc. ATTN: V. Kelsey K. Leighton P.O. Box 6077 Newark, DE 19714-6077
2	Battelle Edgewood Operations ATTN: R. Jameson S. Golaski 2113 Emmorton Park Rd. Edgewood, MD 21040

No. of Copies	Organization
1	Dyna East Corporation ATTN: R. Ciccarelli 3201 Archer St. Philadelphia, PA 19104
2	Institute for Advanced Technology ATTN: S. Bless H. Fair 4030-2 W. Braker Lane Austin, TX 78759-5329
1	Zernow Technical Services, Inc. ATTN: L. Zernow 425 West Benita, Suite 208 San Dimas, CA 91773
1	Orlando Technology, Inc. ATTN: D. Matuska P.O. Box 855 Shalimar, FL 32579
1	Livermore Software Technology Corporation ATTN: J. Hallquist 2876 Waverly Way Livermore, CA 94550

No. of Copies	Organization
1	Ruhr-Universitat Bochum ATTN: J. Kalthoff Universitatstrasse 150 4360 Bochum 1, Postfach 102148 GERMANY
1	Condat GmbH ATTN: K. Thoma Maximilianstrasse 28 8069 Scheyern-Fernhag GERMANY
1	IFAM Materialforschung ATTN: L. Meyer Lesumer Heerstrasse 36 2820 Bremen 77 GERMANY
3	RARDE ATTN: I. Cullis P. Church A. Hopkins Fort Halstead - Sevenoaks TN14 7BP Kent ENGLAND
1	Brunel University BICOM ATTN: J. Whiteman Uxbridge, Middlesex UB8 3PH ENGLAND
1	Defense Research Establishment Suffield ATTN: C. Wickert Ralston, Alberta, TOJ 2NO Ralston CANADA
1	Defense Research Establishment Valcartier ATTN: N. Gass P.O. Box 8800 Courcellette, PQ, GOA 1RO CANADA

No. of Copies	Organization
1	Canadian Arsenals, LTD ATTN: P. Pelletier 5 Montee des Arsenaux Villie de Gardeur, PQ, J5Z2 CANADA
1	Ernst-Mach Institut ATTN: A. Stilp Eckerstrasse 4 D-7800 Freiburg i. Br. GERMANY
1	IABG ATTN: H. Raatschen Einsteinstrasse 20 D-8012 Ottobrun B. Muenchen GERMANY
1	Centre d-Etudes de Vajours ATTN: PLOTARD J.-P. Boite Postale No. 7 77181 Country FRANCE
1	PRB S.A. ATTN: M. Vansnick Avenue de Tervueren 168, Bte. 7 Brussels, B-1150 BELGIUM
1	AB Bofors/Ammunition Division ATTN: Jan Hasslid Box 900 S-691 80 Bofors SWEDEN

INTENTIONALLY LEFT BLANK.